UIC/WEC JOINT RESEARCH PROJECT ON RAIL DEFECT MANAGEMENT

Correlations Between Rail Defect Growth Data and Engineering Analyses, Part II: Field Tests

David Y. Jeong

U.S. Department of Transportation
Research and Special Programs Administration
Volpe National Transportation Systems Center
Cambridge, Massachusetts 02142

January 2003

EXECUTIVE SUMMARY

This report is the second in a three-part series describing the technical contributions of the Federal Railroad Administration (FRA) and the Volpe National Transportation Systems Center (Vole Center) to the UIC/WEC (International Union of Railways/World Executive Council) joint research project on Rail Defect Management. Specifically, this report describes engineering analyses that are used to examine the growth of internal rail defects that were tested under field conditions. The first report in this series describes similar engineering analyses that were conducted to examine the growth of internal rail defects tested under laboratory conditions. The third report discusses some applications of the rail defect modelling work.

The defect growth data described in this report were generated by the Transportation Technology Center, Inc. at the Facility for Accelerated Service Testing in Pueblo, Colorado USA, and by Spoornet in South Africa. Moreover, correlations between the field test data and the results from the engineering fracture mechanics analyses are presented in this report. In general, the correlations between field test data and analysis are reasonable.

The titles of the other reports in this series are:

- Correlations Between Rail Defect Growth Data and Engineering Analyses, Part I: Laboratory Tests.

- Analytical Modelling of Rail Defects and Its Applications to Rail Defect Management.

TABLE OF CONTENTS

Section			Page
1.	INTRODUCTION		1
2.	SUMMARY OF FIELD TESTS		3
3.	DESCRIPTION OF ENGINEERING ANALYSES		7
	3.1	Stress Analysis	7
		3.1.1 Bending Stresses	7
		3.1.2 Thermal Stresses	12
		3.1.3 Residual Stresses	13
	3.2	Fracture Mechanics Analysis	14
		3.2.1 Stress Intensity Factor for Detail Fractures	15
		3.2.2 Crack Growth Rate Equation	18
4.	CORRELATIONS BETWEEN TEST DATA AND MODEL RESULTS		21
5.	DISCUSSION		23
	REFERENCES		29
	APPENDICES		
A.	SECTION PROPERTIES FOR RAIL SAMPLES		A-1
B.	CORRELATIONS BETWEEN FAST FIELD TEST DATA AND RESULTS FROM ENGINEERING ANALYSES		B-1
C.	CORRELATIONS BETWEEN SPOORNET FIELD TEST DATA AND RESULTS FROM ENGINEERING ANALYSES		C-1
D.	UNCORRELATED TEST DATA		D-1

1. INTRODUCTION

Improving railway safety by reducing rail failures and the associated risks of train derailments is an objective of many railroad organizations throughout the world. In 1997, the World Executive Council (WEC) of the Union Internationale des Chemis de fer (UIC, or International Union of Railways) began an international research project on Rail Defect Management.[1] In the present context, rail defect management refers to the development and implementation of strategies for controlling the risk of rail failures.

The primary method for controlling the risk of rail failures is rail testing. Knowledge on the nature of rail defect growth is necessary to determine how often rail tests should be performed. In the UIC/WEC joint research project on Rail Defect Management, studies are being conducted to examine the growth of rail defects under laboratory and revenue service conditions. Engineering fracture mechanics analyses are also being conducted to model the growth behavior observed in the laboratory and field tests.

An engineering analysis model was developed in previous research to estimate the growth rate of a particular type of internal transverse rail defect commonly found in North America, called a detail fracture (Orringer et al., 1988). The model development was sponsored by the Federal Railroad Administration (FRA), and was performed by the Volpe National Transportation Systems Center (Volpe Center). Moreover, this engineering model provides the basis for the analytical work conducted in the UIC/WEC joint research project on Rail Defect Management.

This report is the second in a series that describes correlations between rail defect growth data and results from engineering analyses based on fracture mechanics principles. The first report described the correlations for defect growth data obtained from tests conducted under laboratory conditions (Jeong, 2002). The results presented in the first report show that engineering analyses can provide realistic estimates of the rail defect growth rates observed in the laboratory tests. This report describes similar correlations for rail defect growth data obtained from full-scale, field tests conducted at the Facility for Accelerated Service Testing (FAST) in Pueblo, Colorado USA, and from field tests conducted by Spoornet in South Africa.

FAST is a 4.8-mile (8-kilometer), closed-loop, railroad test track. Several rails containing internal transverse defects were installed in the FAST track. The growth rates of these rail defects were monitored under heavy (39-ton or 35-metric ton) axle loads. Train operations, track maintenance, and test measurements were performed by Transportation Technology Center, Inc. (TTCI), which is a subsidiary of the Association

[1] The organizations participating in the UIC/WEC joint research project on Rail Defect Management are: Association of American Railroads – Transportation Technology Center, China Railways – China Academy of Railway Sciences, East Japan Railways, European Rail Research Institute, India Railways – Research Designs and Standards Organization, Queensland Rail (Australia), Railway Technical Research Institute (Japan), Russian Railway Research Institute, Spoornet (South Africa), and US Department of Transportation – Federal Railroad Administration and Volpe National Transportation Systems Center.

of American Railroads (AAR). The tests at FAST were conducted under the joint sponsorship of the FRA and the AAR.

The growth rates of other internal rail defects were also monitored under revenue service field conditions by Spoornet in South Africa, specifically for the UIC/WEC joint research project on Rail Defect Management.

The purposes of this report are: (1) to provide a brief summary of the FAST and Spoornet field test data; (2) to provide a brief description of the engineering analyses to estimate the growth rate of detail fractures; and (3) to show comparisons between the FAST and Spoornet field test data and results from the engineering fracture mechanics analyses.

2. SUMMARY OF FAST DEFECT GROWTH TESTS

The growth of 37 rail defects were monitored at the Facility for Accelerated Service Testing (FAST) between October 1998 and June 2002. Of these 37 defects, 7 were still in track when this report was being finalized. The data for these rail defects are summarized in Table 1. The initial and final sizes of the internal rail defects are included in the table, and were measured using hand-held ultrasonic equipment. The sizes are given in percent of rail head area (%HA) based on a brand new or unworn rail. The accumulated tonnage is listed in terms of million gross tons (MGT).

The table includes the year of manufacturing for each rail to identify its age. The date of manufacturing provides an indirect indication as to whether the rail was head-hardened or not since several producers of rail had the capability to heat treat rails by the mid 1980s. Experiments to monitor the growth of rail defects were conducted at FAST in the 1980s using rails that were manufactured in the 1970s and were not head-hardened. An objective of the most recent FAST experiments is to determine the effect of head-hardened rails on the rate of rail defect growth.

Most of the tests were performed on curved track. Twelve tests were conducted on tangent track.

The start and end dates for each particular test are included in the table to estimate the climatic conditions during the data collection period. Moreover, the dates are used to obtain actual climatological data (i.e., minimum and maximum daily temperatures) from the U.S. Weather Service,[2] which in turn are used to estimate the thermal stress history for each defect.

Four different rail sections were used in the FAST tests: UIC 60, 132 RE, 133 RE, and 136 RE. The section properties for these rail sections are listed in Appendix A. The section properties are used to calculate rail stresses, which in turn are used to estimate the defect growth rate. The specific details of the stress analysis are described in the following section of the report. The test data for the UIC 60 rail were not correlated with engineering model because no growth was apparent.

Appendix B includes individual comparisons between the FAST defect growth data and the results from the engineering analysis model. All defects in the FAST tests were assumed to be detail fractures in the engineering analyses. Other specific details of the engineering analysis are described in the following section.

[2] Climatological data were obtained from a web site of the Colorado Climate Center, specifically for the Pueblo Weather Service Office, Airport Station (http://climate.atmos.colostate.edu/).

Table 1. Summary of FAST Defect Growth Tests.

Defect No.	Flaw ID	Rail Section	Manuf. Year	Track Curvature	Start Date	End Date	Initial Size (%HA)	Final Size (%HA)	Tonnage (MGT)
1	3A	136 RE	1990	Tangent	Oct 12, 1998	Feb 2, 2000	10.3	2.0	142.82
2	3B	136 RE	1990	Tangent	Oct 12, 1998	Feb 2, 2000	10.0	4.0	142.82
3	2A	136 RE	1991	Curve	Apr 22, 1999	May 21, 1999	8.3	12.0	10.07
4	2B	136 RE	1991	Curve	Apr 22, 1999	May 21, 1999	5.4	37.2	10.07
5	2C	136 RE	1991	Curve	Apr 22, 1999	May 21, 1999	5.4	70.0	10.07
6	2 (5)	132 RE	1987	Curve	May 24, 1999	Nov 18, 1999	15.0	46.0	48.12
7	7	136 RE	1990	Curve	Dec 1, 1999	Feb 16, 2000	12.0	16.5	35.54
8	8	136 RE	1990	Curve	Dec 1, 1999	Feb 16, 2000	3.3	5.8	35.54
9	9	136 RE	1990	Curve	Dec 1, 1999	Feb 16, 2000	8.0	5.4	35.54
10	D	136 RE	1991	Tangent	Dec 8, 1999	Dec 15, 2000	14.8	17.0	2.74
11	F1	136 RE	1990	Tangent	Apr 28, 2000	May 12, 2000	28.1	48.8	6.08
12	F3	136 RE	1990	Curve	Apr 28, 2000	May 15, 2000	6.0	100	8.58
13	F5	132 RE	1979	Tangent	Aug 29, 2000	Sep 12, 2000	21.4	57.7	4.79
14	F6	132 RE	1992	Curve	Aug 29, 2000	Oct 17, 2000	13.7	13.1	27.77
15	F7	132 RE	1992	Curve	Aug 29, 2000	Oct 17, 2000	10.8	47.4	27.77
16	F8	136 RE	1999	Curve	Oct 17, 2000	IN TRACK	8.3		
17	F9	136 RE	1993	Tangent	Jan 25, 2001	Feb 5, 2001	21.0	51.0	7.20
18	A	136 RE	1973	Curve	Oct 24, 2000	Dec 19, 2000	7.2	2.2	23.47
19	B	136 RE	1999	Curve	Oct 24, 2000	Nov 17, 2000	2.8	47.2	14.72
20	C	136 RE	1999	Curve	Oct 24, 2000	Nov 17, 2000	3.0	5.7	14.72
21	D2	136 RE	1999	Curve	Oct 24, 2000	Nov 17, 2000	3.3	5.0	14.72
22	E	136 RE	1999	Curve	Oct 24, 2000	Nov 17, 2000	1.7	13.0	14.72
23	F	136 RE	1998	Curve	Oct 24, 2000	Feb 7, 2002	24.8	50.0	148.76
24	H	UIC 60	1997	Tangent	Oct 24, 2000	Mar 13, 2001	19.4	20.6	63.15
25	J	136 RE	1999	Curve	Jan 12, 2001	Jan 19, 2001	33.5	90.7	3.63
26	K	136 RE	1999	Curve	Apr 19, 2001	May 3, 2001	20.0	61.0	8.86
27	O	136 RE	1990	Tangent	Feb 2, 2001	IN TRACK	4.0		
28	M	136 RE	1993	Curve	Mar 13, 2001	IN TRACK	2.2		
29	N	136 RE	1993	Curve	Mar 13, 2001	IN TRACK	4.1		
30	I	136 RE	1997	Tangent	Jul 27, 2001	IN TRACK	8.3		
31	F10	136 RE	1987	Curve	Aug 29, 2001	IN TRACK	3.1		
32	GT12	136 RE	1973	Tangent	Aug 29, 2001	Nov 8, 2001	5.2	33.0	5.81
33	P	136 RE	1993	Tangent	Aug 29, 2001	IN TRACK	0.7		
34	F11	136 RE	1975	Tangent	Dec 13, 2001	Jan 21, 2002	12.4	65.0	6.45
35	Q	136 RE	1993	Curve	Jan 24, 2002	Mar 15, 2002	19.3	30.0	31.40
36	R	136 RE	1993	Curve	Jan 24, 2002	Mar 15, 2002	19.3	24.0	31.40
37	S	133 RE	1998	Curve	Feb 4, 2002	Feb 27, 2002	15.0	83.0	14.89

Blue = Correlated Black = Uncorrelated Red = In track

Tests were also performed by Spoornet to monitor the growth of internal rail defects under revenue service field conditions. Table 2 provides a summary of seven tests which were conducted from July 2001 to January 2002. Internal rail defects were identified by an ultrasonic detector car, and verified with a hand-held instrument. The growth of these defects was monitored using a hand-held, 70-degree, double-crystal probe. The defects were removed from revenue service as soon as the measured size reached 12 to 13 mm.[3] Each defect was found in a UIC 60 rail section. All of the defects was located in either tangent track or extremely gentile curved track.

Appendix C shows comparisons between the Spoornet defect growth data and the results from the engineering analysis model. All defects in the Spoornet tests were assumed to be tache ovale defects.

In some cases involving the FAST growth tests, the data were not correlated with the engineering analysis model because no growth was evident. The data for these particular cases are plotted, and included in Appendix D.

[3] After removal from revenue service track, the rail samples were then tested in the laboratory to monitor the defect growth rate under controlled conditions. The laboratory test data and the corresponding engineering analyses are described in a separate report (Jeong, 2002).

Table 2. Summary of Spoornet Field Tests.

Defect No.	Rail Section	Track Curvature	Flaw Size (mm)		Cycles	Start Date	End Date
			Initial	Final			
1432	UIC 60	Tangent	4	13	1.04×10^5	30-Jul-01	15-Aug-01
1435	UIC 60	Tangent	5	13	1.21×10^6	30-Jul-01	22-Jan-02
1454	UIC 60	1.2E Curve	7	13	2.49×10^5	30-Jul-01	5-Sep-01
1456	UIC 60	0.9E Curve	9	13	9.68×10^4	30-Jul-01	14-Aug-01
1601	UIC 60	1.2E Curve	9	11	8.57×10^5	3-Aug-01	6-Dec-01
1614	UIC 60	0.5E Curve	9	11	8.64×10^5	2-Aug-01	6-Dec-01
1628	UIC 60	Tangent	9	13	8.64×10^5	2-Aug-01	6-Dec-01

3. DESCRIPTION OF ENGINEERING ANALYSES

In previous research, an engineering analysis model was developed to facilitate consistent and realistic estimates of the slow crack-growth life of detail fractures under conditions representative of revenue service (Orringer et al., 1988).[4] In this context, the slow crack-growth life refers to the time or tonnage to grow a rail defect from detectable size to the size at which rail failure may be expected to occur under the next train. Moreover, the slow crack-growth life represents the time or tonnage during which the rate of crack growth is predictable under normal conditions. The same engineering analysis model was used in the present work to correlate the rail defect growth data obtained from the FAST and Spoornet tests.

3.1 STRESS ANALYSIS

The growth of rail defects is driven by the cyclic variation of live-load stress due to rail bending. Thermal and residual stress effects also contribute to the propagation of rail defects. Engineering analyses are applied to estimate the longitudinal stress in the rail due to train traffic. In these analyses, the longitudinal component of stress consists of three parts: (1) live-load bending stress, (2) thermal stress, and (3) residual stress.[5]

3.1.1 Bending Stresses

The stresses produced by bending of the rail are calculated using a beam-theory analysis (Timoshenko and Langer, 1932). In this analysis, the rail is assumed to behave as a continuous beam supported by elastic foundations in the vertical, lateral, and rotational directions. Moreover, the longitudinal bending stress in the rail head is assumed to comprise five components: (1) vertical bending, (2) lateral bending, (3) warping, (4) vertical head-on-web bending, and (5) lateral head-on-web bending.

Vertical and Lateral Bending

Vertical and lateral bending of the rails is based upon the assumption that the rail can be considered as a beam that is continuously supported by an elastic foundation (e.g., see Hetenyi, 1983). The distributions of the vertical and lateral bending moments along the rail are given mathematically as

[4] A detail fracture is a transverse defect originating near the surface of the rail head. Detail fractures account for about 75% of the rail defect population in continuous welded rail track in North America.

[5] Stresses are also produced from the contact pressure between the rail and the wheel. Contact stresses typically decay completely within 1 inch of the wheel/rail interface. Rail defects are generally located deep enough below the running surface so that contact stresses can be neglected.

$$M_V(x) = \frac{V}{4b_V} e^{-b_V x} \left(\cos b_V x + \sin b_V x \right) \tag{1}$$

$$M_L(x) = \frac{L}{4b_L} e^{-b_L x} \left(\cos b_L x + \sin b_L x \right) \tag{2}$$

where V is the vertical wheel load and L is the lateral wheel load. Also,

$$b_V = \sqrt[4]{\frac{k_V}{4EI_{yy}}} \tag{3}$$

$$b_L = \sqrt[4]{\frac{k_L}{4EI_{zz}}} \tag{4}$$

where I_{yy} is the vertical bending inertia of the entire rail, I_{zz} is the lateral bending inertia of the entire rail, k_V is the vertical foundation modulus, k_L is the lateral foundation modulus, and E is the modulus of elasticity for rail steel ($3H10^7$ psi assumed).

The longitudinal stress component due to vertical bending is

$$s_V(x) = \frac{M_V(x) z}{I_{yy}} \tag{5}$$

where z is the vertical location of the point of interest relative to the rail neutral axis. Similarly the longitudinal stress component due to lateral bending is

$$s_L(x) = \frac{M_L(x) y}{I_{zz}} \tag{6}$$

where y is the lateral location of the point of interest relative to the rail neutral axis.

Constrained Warping

Warping or twisting of the rail occurs from eccentric vertical and lateral wheel loads. Since the rail is constrained, the twisting of the rail is accompanied by a bending of the head and base of the rail. The warping stress is calculated using the following equation:

$$s_W(x) = Eh_1 y \frac{d^2 j}{dx^2} \tag{7}$$

where y is the lateral location of the point of interest relative to the rail neutral axis and f is the angle of twist. The second derivative of the angle of twist can be derived from the beam on elastic foundation theory:

$$\frac{d^2 j}{dx^2} = \frac{Lf - Ve}{4Dh^2 b_1 b_2} e^{-b_1 x} \left[b_1 \sinh(b_2 x) - b_2 \cosh(b_2 x) \right] \tag{8}$$

where e and f define the location of the vertical and lateral wheel loads relative to the shear center of the rail (see Figure 1).

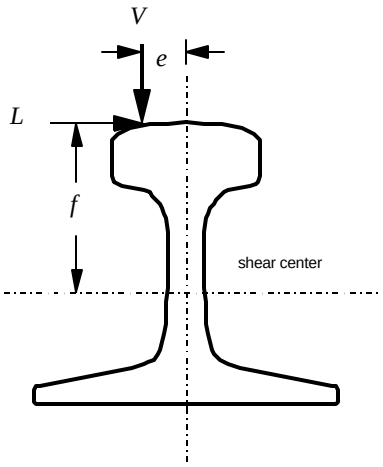

Figure 1. Rail subjected to eccentric vertical and lateral wheel loads.

In equation (8),

$$b_1 = \sqrt{\frac{C}{4Dh^2} + \sqrt{\frac{k_t}{4Dh^2}}} \tag{9}$$

$$b_2 = \sqrt{\frac{C}{4Dh^2} - \sqrt{\frac{k_t}{4Dh^2}}} \tag{10}$$

where k_t is the torsional foundation modulus (10^5 lb per radian assumed), h is the distance between the centroids of the head and the base, C is called the torsion constant, and D is called the warping constant. The torsion and warping constants are calculated from:

$$C = \frac{GA_R^2}{40J_C} \tag{11}$$

$$D = E\frac{I_{zzB}I_{zzH}}{I_{zzB}+I_{zzH}} \tag{12}$$

where G is the shear modulus of elasticity for rail steel (1.154×10^7 psi assumed), A_R is the cross-sectional area of the entire rail, J_C is the polar moment of inertia of the entire ail about the shear center, I_{zzB} is the lateral bending inertia of the rail base alone, and I_{zzH} is the lateral bending inertia of the rail head alone. The polar moment of inertia about the shear center is calculated from:

$$J_C = I_{yy} + I_{zz} + A_R\left(h_N - h_C\right)^2 \tag{13}$$

where h_N is the height of the centroid of the entire rail and h_C is the height of the shear center. In equation (7),

$$h_1 = h\frac{I_{zzB}}{I_{zzB}+I_{zzH}} \tag{14}$$

Head-On-Web Bending

Head-on-web bending refers to bending of the head alone. Since the head is wider and stiffer than the web, the rail head is considered as a separate beam bending on the elastic foundation formed by the web. For vertical bending, the effective modulus of foundation of the web is

$$k_{V_{how}} = \frac{t_w}{h_w}E \tag{15}$$

where t_w is the average web thickness and h_w is the web height. For lateral bending, the effective foundation modulus of the web is

$$k_{L_{how}} = \left(\frac{t_w}{h_w}\right)^3 E \tag{16}$$

The moments for vertical and lateral head-on-web bending are

$$M_{Vhow}(x) = \frac{V}{4b_{Vhow}}e^{-b_{Vhow}x}\left(\cos b_{Vhow}x + \sin b_{Vhow}x\right) \tag{17}$$

$$M_{Lhow}(x) = \frac{L}{4b_{Lhow}}e^{-b_{Lhow}x}\left(\cos b_{Lhow}x + \sin b_{Lhow}x\right) \tag{18}$$

where

$$b_{Vhow} = \sqrt[4]{\frac{k_{Vhow}}{4EI_{yyH}}} \tag{19}$$

$$b_{Lhow} = \sqrt[4]{\frac{k_{Lhow}}{4EI_{zzH}}} \tag{20}$$

In equations (19) and (20), I_{yyH} and I_{zzH} are the vertical and lateral bending inertias of the rail head only. The vertical and lateral head-on-web bending stresses are calculated from:

$$s_{Vhow}(x) = \frac{M_{Vhow}(x) z_1}{I_{yyH}} \tag{21}$$

$$s_{Lhow}(x) = \frac{M_{Lhow}(x) y_1}{I_{zzH}} \tag{22}$$

where z_1 and y_1 are the vertical and lateral locations of the point of interest relative the neutral axis of the rail head only.

Dynamic Effects

Dynamic motions of vehicles (pitch, bounce, and rocking) cause fluctuations in the magnitude of vertical wheel loads on the rail as trains travel over the track. The dynamic effect is assumed to increase with train speed. Moreover, the dynamic vertical wheel load is assumed to be the static wheel load multiplied by a magnification factor that depends on train speed. The American Railroad Engineering Association (AREA) has recommended the following dynamic load factor:

$$DLF = 1 + \frac{33v}{100d} \tag{23}$$

where v is the train speed (in miles per hour or mph) and d is the wheel diameter (in inches).

The normal operating train speed at FAST is 40 mph, or 24 kilometers per hour. The dynamic load factor corresponding to this train speed and a freight wheel diameter of 36 inches is 1.367. Therefore, the dynamic vertical load for a 33-kip static wheel load traveling at a speed of 40 mph is slightly more than 45 kips. The average train speed on a coal line in South Africa is 100 mph, or 60 kilometers per hour. Assuming a 36-inch wheel diameter, the corresponding dynamic load factor is 1.917.

Total Longitudinal Bending Stress

The total longitudinal bending stress in the rail head is the sum of five components. If dynamic effects are included in the stress calculation, the sum is multiplied by the dynamic load factor:

$$s_B(x) = DLF\left[s_V(x) + s_L(x) + s_W(x) + s_{Vhow}(x) + s_{Lhow}(x)\right] \quad (24)$$

where x is the longitudinal distance along the rail.

Figure 2 shows a schematic of longitudinal bending stresses along the rail that are produced by the wheel loads from the ends of two adjacent trucks on two equally loaded hopper cars (with 70-inch wheel spacing, 434.4-inch truck-center spacing, and 585-inch length over the couplers). The valleys and peaks of this variation define the minimum (as denoted by the solid circles in Figure 2) and the maximum (denoted by the solid squares) bending stresses, respectively, which in turn define a stress cycle. Thus, the four wheel loads shown in the figure produce 5 stress cycles (5 pairs of minimum and maximum stresses).

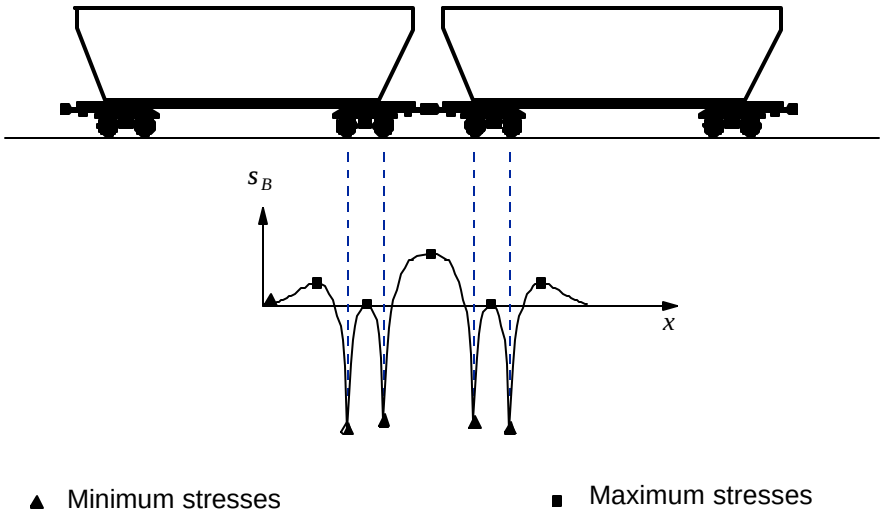

Figure 2. Bending cycles produced by adjacent ends of coupled hopper cars.

3.1.2 Thermal Stresses

Thermal stresses develop in continuous welded rail (CWR) through the difference between the rail neutral temperature[6] and the rail service temperature. In fully restrained CWR in tangent track, thermal stress can be calculated using the following formula:

[6] Neutral temperature is defined as the temperature at which the net longitudinal force in the rail is zero.

$$s_T = Ea\left(T_N - T\right) \tag{25}$$

where E is the modulus of elasticity, a is the coefficient of thermal expansion, T_N is the rail neutral temperature, and T is the rail service temperature. For nominal properties of rail steel, Ea in equation (25) is equal to 0.195 ksi per degree Fahrenheit, or 2.4 MPa per degree Celsius.

Thermal stresses fluctuate in response to daily and seasonal changes in both the rail service temperature and the rail neutral temperature (Kish et al., 1987). In principle, thermal stress cycles can drive the propagation of rail defects. In practice, however, one year of thermal stress cycles generally has somewhat less effect than the live-load stress cycles from one train. It is reasonable to neglect thermal stress cycles, therefore, and to consider only the effect of thermal stress as a slowly varying mean stress that is superimposed on the live-load stress cycles.

The variation of rail neutral temperature in both time and location along the track depends on the interaction of such diverse factors as track disturbance during tamping, local distressing of CWR strings when individual rails are replaced, roadbed freeze-thaw cycles, the rolling out of rails by plastic deformation in the rail head caused by wheel-rail contact loads, and the dynamic forces exerted on the rails by passing trains.

The U.S. Weather Service publishes daily weather records which include high and low ambient temperature, precipitation, and other data for numerous locations. The data from such records can be used to estimate rail service temperature histories. For example, the daily high rail service temperature can be estimated as 30°F above the daily ambient high when the weather conditions are described as sunny in Pueblo, Colorado.

3.1.3 Residual Stresses

Residual stresses are those that remain in an externally unloaded rail. The distribution of the longitudinal residual stress in the rail head is complex, and varies from one rail to another. A feature observed from measurements of residual stress is the existence of residual tension in the region where internal defects originate and grow. The magnitude of the largest tensile residual stress also can vary from one rail to another. Moreover, the residual tension promotes the growth of rail defects.

As a simplifying assumption in the present engineering analyses, a uniform residual stress is assumed in place of a distribution. Furthermore the uniform residual stress is assumed to decrease as the rail defect enlarges. Figure 3 shows an empirically derived relation between the uniform residual tension and defect size for detail fractures (Clayton and Tang, 1992). The physical interpretation of this relation is that the residual stresses are relieved by the creation of fracture surfaces as the defect grows.

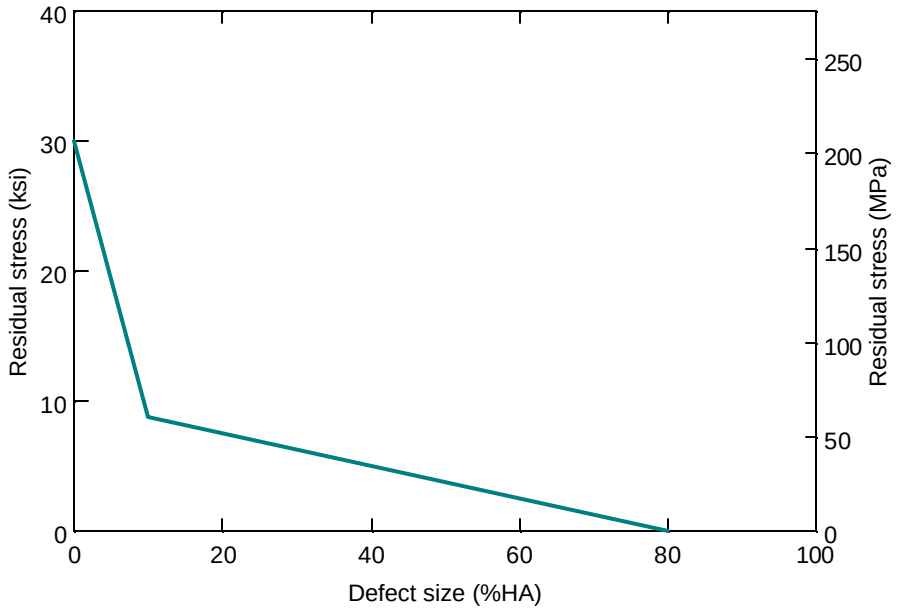

Figure 3. Empirical relation between uniform residual stress and defect size.

In the analyses described in this report, the residual stresses depend on the defect size, and are calculated using the follows equation:

$$s_R = \begin{cases} SF\left(30 - 2.125A\right) & \text{if } 0\% \le A < 10\% \\ SF\left(10 - 0.125A\right) & \text{if } 10\% \le A \le 80\% \end{cases} \tag{26}$$

where A is the defect size in percent rail head area (%HA) and SF is referred to as the severity factor. Moreover, the severity level is a multiplying factor on the residual stress curve shown in Figure 3. Physically the severity factor accounts for the variation in residual stresses from one rail to another.

3.2 FRACTURE MECHANICS ANALYSIS

In engineering fracture mechanics analyses, the state of stress in the vicinity of a crack or defect is characterized by the stress intensity factor or "*K*" formula. Stress intensity factor formulas have been derived for a variety of crack geometries from the classical theory of elasticity (e.g., Sih, 1973). Established stress intensity factors were modified in previous research to develop *K*-formulas for detail fractures (Orringer, et al., 1988).

3.2.1 Stress Intensity Factor for Detail Fractures

The detail fracture is modeled with two basic "*K*" formulas (Figure 4). One "*K*" formula is for a circular crack embedded in an unbounded body to represent defects up to 50%HA. The other is for a quarter-circular crack embedded in a quarter-space body to represent larger defects that have broken out to the gage face and/or running surface. The basic "*K*" formulas were modified with empirical factors to represent the non-circular shapes of typical detail fractures before breakout and to account for the finite dimensions of the rail cross section.

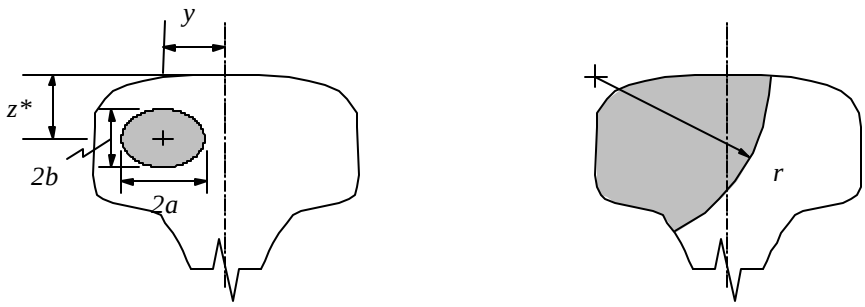

(a) Penny Crack ***(b) Corner Crack***

Figure 4. Modelling of detail fractures.

The stress intensity factor formula for the elliptical-shaped internal detail fracture in the rail head is given by:

$$K = \frac{2}{p} M_1 M_S \left(s_R + s_T + M_G s_B \right) \sqrt{p\, a} \qquad (27)$$

where a is the semi-major axis length of the elliptical crack, M_1 is an empirical factor for the finite dimensions of the rail cross section, M_S is an empirical factor to account for the non-circular shape of the defect, M_G is an empirical factor to account for stress gradients in the rail head, s_R is the average residual stress, s_T is the thermal stress, and s_B is the live-load bending stress.

Figure 5 shows that the empirical factor to account for the non-circular (i.e., elliptical) shape of the defect varies between 0.9 and 1.0 for aspect ratios between 0.4 and 1.0. The aspect ratio of the elliptical flaw is defined as the ratio of the semi-minor axis length to the semi-major axis length (see Figure 4). In the present analyses, an aspect ratio of 0.7 is assumed for detail fractures which corresponds to an empirical factor of 0.984. An aspect ratio of 0.83 is assumed for tache ovale defects, corresponding to an empirical factor of 0.996.

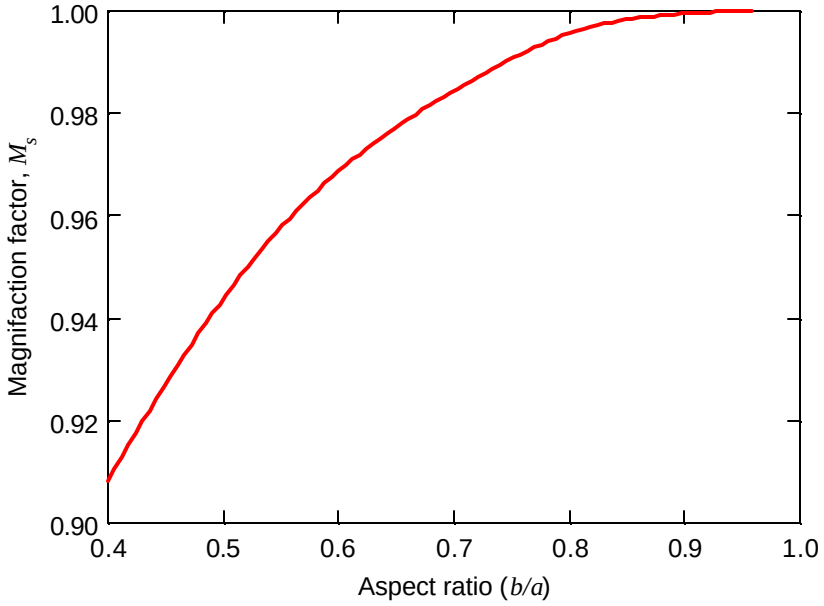

Figure 5. Empirical factor to account for non-circular defect shape.

The magnification factor to account for the finite cross section of the rail head is

$$M_1 = \sqrt{\frac{200}{pA}\tan\left(\frac{pA}{200}\right)}\,\frac{0.63 + 0.0202A + 0.37\left[1-\sin\left(\frac{pA}{200}\right)\right]^3}{\cos\left(\frac{pA}{200}\right)} \tag{28}$$

where A is the defect size in percent rail head area (%HA).

The stress-gradient magnification factor is calculated from the following equations:

$$M_G = \left[\frac{\int_0^{2p} M_{pc}(J)^p\, r(J)\, dJ}{\int_0^{2p} r(J)\, dJ}\right]^{1/p} \tag{29}$$

where p is the exponent in the crack growth rate equation (discussed later in this section). Equation (29) contains two auxiliary functions, which are defined as:

$$r(J) = \frac{b}{\sqrt{\sin^2 J + (b/a)\cos^2 J}} \tag{30}$$

$$M_{pc}(J) = \frac{M_V(J) + \frac{y}{z}\frac{b_V}{b_L}\frac{I_{yy}}{I_{zz}}\frac{L}{V}M_L(J)}{1 + \frac{y}{z}\frac{b_V}{b_L}\frac{I_{yy}}{I_{zz}}} \tag{31}$$

where I_{yy} and I_{zz} are the vertical and lateral bending inertias of the entire rail, y and z are the lateral and vertical locations of the center of the defect relative to the neutral axis, and b_V and b_L were defined previously in equations (3) and (4). Also, L/V is the ratio of the lateral to vertical wheel loads. The other functions in equation (31) are

$$M_V(J) = 1 + \frac{(b/z)k^2 E_I(k)\sin J}{(1+k^2)E_I(k) + (1-k^2)E_{II}(k)} \tag{32}$$

$$M_L(J) = 1 + \frac{(a/y)k^2 E_I(k)\cos J}{(1-2k^2)E_I(k) - (1-k^2)E_{II}(k)} \tag{33}$$

where $k^2 = 1-(b/a)^2$. In equations (32) and (33), E_I and E_{II} are the complete elliptic integrals of the first and second kind, which are defined mathematically as

$$E_I(k) = \int_0^{p/2} \sqrt{1-k^2\sin^2 J}\; dJ \qquad\qquad E_{II}(k) = \int_0^{p/2} \frac{dJ}{\sqrt{1-k^2\sin^2 J}} \tag{34}$$

Since equation (31) refers to the vertical and lateral bending inertias, I_{yy} and I_{zz}, the stress-gradient magnification factor depends not only on the lateral-to-vertical wheel load ratio (L/V), but on the rail section as well.

The location of the center of the defect relative to the top of the rail (Figure 4) is calculated from an empirical relation derived from previous research

$$z^* = 0.6213 + 1.7580\times10^{-2} A - 1.7933\times10^{-4} A^2 \tag{35}$$

where A is the defect size in percent rail head area (%HA) and z^* is in inches. Similarly, an empirical relation was also derived for the location of the center of the defect relative to the vertical centerline of the rail

$$y = 1.1874 - 2.9523\times10^{-2} A + 3.4306\times10^{-4} A^2 \tag{36}$$

where y is in inches. For detail fractures that have broken out to the gage face and running surface, the stress intensity factor formula is given by:

$$K = \frac{2}{p} M_1 \left(s_R + s_T + M_G s_B \right) \sqrt{p\, r} \tag{37}$$

where r is the radius of the quarter-circular crack (see Figure 4). The magnification factor to account for the finite cross section is similar but slightly different than the previous case. For larger detail fractures, the finite-section magnification factor is

$$M_1 = \sqrt{\frac{200 A_X}{p\, A} \tan\left(\frac{p\, A}{200 A_X} \right)} \frac{0.83 + 0.0202 \frac{A}{A_X} + 0.37 \left[1 - \sin\left(\frac{p\, A}{200 A_X} \right) \right]^3}{\cos\left(\frac{p\, A}{200 A_X} \right)} \tag{38}$$

where A is the defect size in percent rail head area (%HA), and $A_X = 1 + 0.5 A_R / A_H$.

In this case, the stress-gradient magnification factor for relatively large detail fractures is given by

$$M_G = \left[\frac{2}{p} \int_0^{p/2} M_{cc}(J)^P \, r(J) \, dJ \right]^{1/p} \tag{39}$$

where $r(J)$ is defined by equation (30), and

$$M_{cc}(J) = \frac{1 + \frac{w_H}{2 z_1} \frac{b_V}{b_L} \frac{I_{yy}}{I_{zz}} \frac{L}{V} \left(1 - \frac{4}{3} \frac{r}{w_H} \cos(J) \right)}{1 + \frac{w_H}{2 z_1} \frac{b_V}{b_L} \frac{I_{yy}}{I_{zz}} \frac{L}{V}} \tag{40}$$

In this equation, w_H is the rail head width and z_1 is the distance between the upper gauge corner of the rail head and the rail neutral axis. The subscript '*cc*' in equation (40) is used to denote that corner crack. In equation (31), the subscript '*pc*' is used to denote penny crack.

3.2.2 Crack Growth Rate Equation

Fatigue crack propagation is assumed to be proportional to the stress intensity factor range (or difference between the maximum and minimum stress intensity factors in a given stress cycle) raised to a power. In the present work, the growth of detail fractures in the rail head is calculated using the following equation:

$$\frac{d\ell}{dN} = C\frac{\Delta K^p}{(1-R)^q} \tag{41}$$

where ℓ is the characteristic defect size (i.e., a for the penny crack or r for the corner crack), N is the number of cycles, DK is the stress intensity factor range, and R is the stress ratio (defined as the ratio of minimum to maximum stress in a given stress cycle). Equation (41) also includes material constants C, p, and q that must be determined through laboratory experiments. Table 3 lists the values of these empirical constants that were derived from experiments conducted for plain carbon rail steel (Scutti et al., 1984).

Table 3. Empirical Constants for Crack Growth Rate Equation.

C		p	q
(SI units)	(English units)		
1.74×10^{-13} m-(MPa-m$^{1/2}$)$^{-4}$-cycle^{-1}	1.00×10^{-11} inch-(ksi-inch$^{1/2}$)$^{-4}$-cycle^{-1}	4	1.63

By treating equation (41) as a separable ordinary differential equation, the number of cycles to grow a crack from an initial size ℓ_i to a larger size ℓ_f can be calculated from

$$N = \frac{1}{C}\int_{\ell_i}^{\ell_f} \frac{(1-R(\ell))^q}{\left(G(\ell)\Delta s\,(\ell)\sqrt{p\,\ell}\right)^p}\,d\ell \tag{42}$$

where Ds and R are the stress range and the stress ratio, which depend on the defect size. Also, G refers to a geometry function, which for the so-called penny crack is

$$G(\ell) = \frac{2}{p}M_S M_1(\ell) \tag{43}$$

where M_S is the shape magnification factor and M_1 is the finite-section magnification factor defined by equation (28). The stress range and stress ratio are defined as

$$\Delta s = s_{B\max} - s_{B\min} \tag{44}$$

$$R = \frac{s_R + s_T + M_G s_{B\min}}{s_R + s_T + M_G s_{B\max}} \tag{45}$$

where s_{Bmin} and s_{Bmax} are the minimum and maximum live-load bending stresses in a given cycle.

The geometry function for the corner crack is

$$G(\ell) = \frac{2}{p} M_1(\ell) \tag{46}$$

where M_1 in this case is defined by equation (38).

In the calculation of slow crack-growth life, the detail fracture is assumed to be an embedded elliptical flaw, or penny crack, when its size is less than or equal to 30 %HA. The detail fracture is assumed to be a corner crack when its size is greater than or equal to 50 %HA. When its size is between 30 and 50 %HA, the detail fracture is assumed to be a combination of the two cracks:

$$N = \begin{cases} N_{pc} \text{ if } A \le 30\%\text{HA} \\ \left(\frac{50 - A}{20}\right) N_{pc} + \left(\frac{A - 30}{20}\right) N_{cc} \text{ if } 30\%\text{HA} < A < 50\%\text{HA} \\ N_{cc} \text{ if } A \ge 50\%\text{HA} \end{cases} \tag{47}$$

4. CORRELATIONS BETWEEN TEST DATA AND MODEL RESULTS

The defect growth data collected from the FAST tests were calibrated with the engineering fracture mechanics model by treating the residual stress severity factor in equation (26) as a scaling factor. Table 4 summarizes the correlations between the FAST test data for 20 defects and the engineering model. The table lists the residual stress severity factors for which the engineering model provides the best fit for each particular test, and Pearson's correlation coefficient[7] which quantifies the goodness of fit. The last column in the table describes the assumptions made in the engineering analysis regarding thermal stress.

Table 4. Summary of Correlations Between FAST Data and Engineering Model.

Flaw ID	*Rail Section*	*Residual Stress Severity Factor, SF*	*Correlation Coefficient, r*	*Comments*
2A	136 RE	0.34	0.225	Constant s_T = 5 ksi
2B	136 RE	1.00	0.930	Constant T_N = 78EF
2C	136 RE	1.25	0.927	Constant T_N = 78EF
5	132 RE	0.70	0.879	Constant s_T = 0 ksi
D	136 RE	0.84	0.832	Constant s_T = 2 ksi
F1	136 RE	0.93	0.882	Actual thermal stress
F3	136 RE	1.10	0.937	Actual thermal stress
F5	132 RE	0.73	0.878	Actual thermal stress
F7	132 RE	0.65	0.623	Actual thermal stress
F9	136 RE	1.15	0.767	Actual thermal stress
B	136 RE	0.95	0.947	Constant T_N = 80EF
C	136 RE	0.30	0.527	Constant T_N = 80EF
E	136 RE	0.60	0.731	Constant T_N = 80EF
J	136 RE	0.48	0.693	Constant T_N = 65EF
K	136 RE	0.55	0.909	Constant T_N = 80EF
GT2	136 RE	1.50	0.348	Constant T_N = 80EF
F11	136 RE	1.50	0.920	Constant T_N = 80EF
Q	136 RE	0.33	0.768	Constant s_T = 1 ksi
R	136 RE	0.30	0.495	Constant s_T = 0 ksi
S	133 RE	1.00	0.884	Constant s_T = 2 ksi

[7] Pearson's correlation coefficient is a quantitative index of the strength of a linear relationship between two variables. It can take on values between –1 and +1; where –1 is perfect negative correlation, 0 is no correlation, and +1 is perfect positive correlation. A correlation coefficient with no sign at all indicates a positive correlation.

Strain gauge data were collected in addition to flaw sizing measurements in all tests. In five cases, enough strain gauge data were available to estimate the complete thermal stress history of the defect during the duration of the test. In most of the other cases, the data were limited (i.e., malfunctioning strain gauge, not enough measurements, etc.), so that other assumptions were necessary to conduct the engineering analysis. In such cases, either the rail neutral temperature or the thermal stress was assumed in the analysis. The effect of these assumptions is discussed in the next section.

Comparisons between the FAST test data and results from the engineering analyses for each defect listed in Table 4 are shown in Appendix B.

Table 5 summarizes the correlations between the Spoornet field test data and the engineering analyses. In the stress analysis for the Spoornet tests, the foundation modulus was assumed to be 10,000 psi to represent concrete ties, and the average train speed was assumed to be 60 kilometers per hour or 100 miles per hour. Moreover, the rails used in the Spoornet tests were assumed to contain tache ovale defects.

Table 5. Summary of Correlations Between Spoornet Data and Engineering Model.

Defect No.	*Rail Section*	*Residual Stress Severity Factor, SF*	*Correlation Coefficient, r*
1432	UIC 60	1.8	0.851
1435	UIC 60	0.4	0.784
1454	UIC 60	0.8	0.878
1456	UIC 60	1.3	0.696
1601	UIC 60	0.2	0.706
1614	UIC 60	0.1	0.672
1628	UIC 60	0.3	0.926

Comparisons between the Spoornet field test data and results from the engineering analyses for each defect listed in Table 5 are shown in Appendix C.

5. DISCUSSION

Table 4 summarizes the correlations for 20 defects tested at FAST in the USA. These defects were assumed to be detail fractures. Table 5 summaries the correlations for seven defects tested by Spoornet in South Africa. In the Spoornet field tests, the defects were assumed to be tache ovale defects. The correlation coefficients listed in both tables vary between 0.225 and 0.947. In all but six cases, the correlation coefficient is greater than 0.7. A correlation coefficient greater than 0.7 indicates a strong association between test data and model results. In general, the residual stress severity levels appear to be reasonable. The severity levels vary between 0.3 and 1.8, which correspond to maximum tensile longitudinal residual stresses of 9 and 54 ksi.

The data from ten tests conducted at FAST were not correlated with the engineering analysis model because no growth was evident. The data for these particular cases are shown in Appendix D. Large variations in defect size at the same tonnage level were evident in some cases that were correlated and not correlated with the engineering analysis model. These variations in defect sizing may partly explain the weak correlation between test data and analysis in the cases where the correlation coefficient was less than 0.7.

The first report in this series (Jeong, 2002) showed correlations between laboratory test data and engineering analyses. The correlation coefficients presented in the previous report are generally higher than those listed in Table 4 and 5. A possible reason for this is that the variations in defect sizing in the field tests were larger than those in the laboratory tests. Another reason is that modelling of the field tests requires additional assumptions to account for the uncertainties that did not exist in the laboratory tests. For example, the contact position of the wheel load on the rail has been assumed in the stress analysis to remain constant (under field service conditions the contact position is known to wander laterally across the rail head). Also, thermal stresses are known to have a significant effect on defect growth rate, but are estimated from climatological data for each defect. Although such assumptions were required in the analysis of the FAST and Spoornet data, the correlations between test and analysis appear to be reasonable.

Sizing of the internal rail defects was performed with hand-held ultrasonic (UT) equipment. A hypothesis for the variations in defect sizing is that UT sizing is affected by changes in rail temperature. Rail temperatures greater than the neutral temperature create compressive rail forces which press the opposing fracture surfaces together and close the crack. Touching of the crack surfaces allows for partial transmission of the ultrasonic beam. Consequently crack closure would result in the ultrasonic equipment underestimating the actual defect size.

Train operations at FAST routinely shutdown every year between June and September as a precaution to avoid buckling under a moving train. No tonnage is accumulated during the shutdown period, but defect sizing measurements were continued daily. Although thermal stresses are present in the rail, the growth of internal defects due purely to

thermal stress variations is unlikely.[8] Therefore the data collected during the shutdown period can be used to test the notion of crack closure affecting ultrasonic sizing. Data collected during the summer of 1999 for four different rail defects are plotted as ultrasonic (UT) defect sizing measurement as a function of rail temperature in Figure 6. The rail temperatures during that time varied between 54 and 134 degrees Fahrenheit. The average sizes for the two defects shown in Figure 6(a) and (b) are 3.1 and 5.2 %HA. The other two defects coincidently have the same average size of 11.8 %HA. Moreover, these scatter plots do not appear to show any correlation between the UT defect sizing measurement and rail temperature.

The actual thermal stress history was estimated from the strain gauge data for five defects (see Comments column in Table 4). In the remaining FAST field tests, the strain gauge data were either unavailable or appeared to be questionable. In such cases, either the rail neutral temperature or the thermal stress was assumed in the engineering analysis. Moreover, in either case, the rail neutral temperature or the thermal stress was assumed to remain constant during the duration of the test. The assumption of constant thermal stress is an oversimplification, but may be acceptable if the average daily rail temperature over the test duration is relatively constant.

The effect of the various assumptions regarding rail neutral temperature and thermal stress is examined by exercising the model for a case where the rail neutral temperature history was known from the strain gauge data.

The variation in rail neutral temperature during the testing of FAST Flaw F1 is shown in Figure 7. The symbols in the figure indicate values of rail neutral temperature as calculated from the strain gauge data. The figure indicates that minimum and maximum rail neutral temperatures were 70.9 EF and 82.5 EF. The average rail neutral temperature during the duration of this particular test was 75.9 EF.

Figure 8 shows that the engineering model results for FAST Flaw ID F1 are roughly the same when the neutral temperature is assumed to be constant (and equal to the average of 76 EF) and when it is assumed to vary according to the measured data. The figure also shows results from assuming a constant thermal stress of 3 ksi during the duration of the test. The residual stress severity factor was equal to 0.93 for each curve in the figure.

Figure 9 shows the calculated growth curves for different assumed values of constant rail neutral temperature. Most of the data points lie within the bounds of the extremes.

Figure 10 shows the calculated growth curves for different assumed values of constant thermal stress. The thermal stress is varied "2 ksi from the baseline value of 3 ksi. This figure also shows that most of the data points lie within the bounds of the extremes. It also indicates that thermal stress has a strong effect on the defect growth rate.

[8] One year of thermal cycles generally has somewhat less effect on defect growth than the live-load stress cycles from one train (Orringer, et al., 1988).

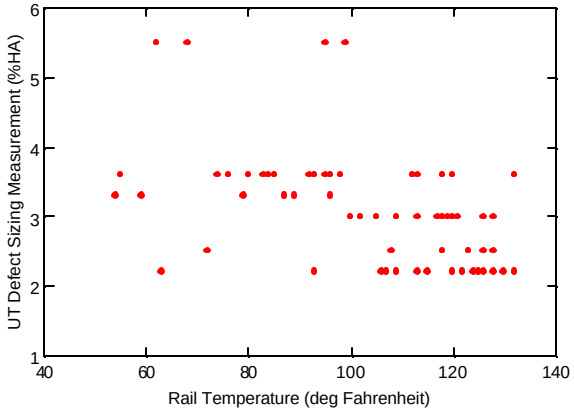

(a) Flaw 3A

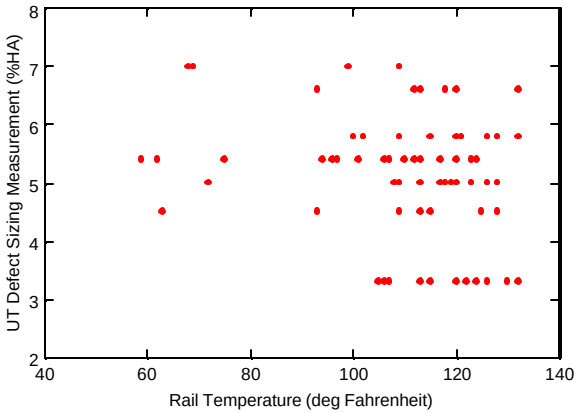

(b) Flaw 3B

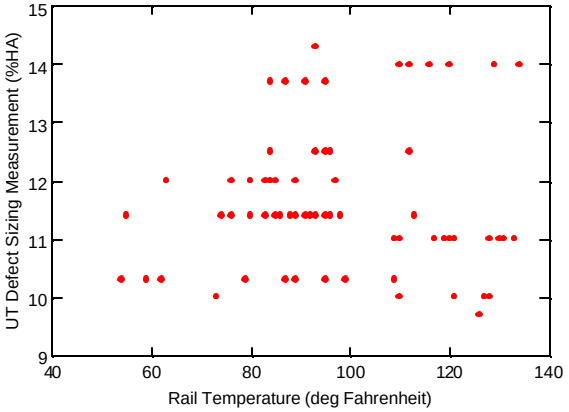

(c) Flaw 5

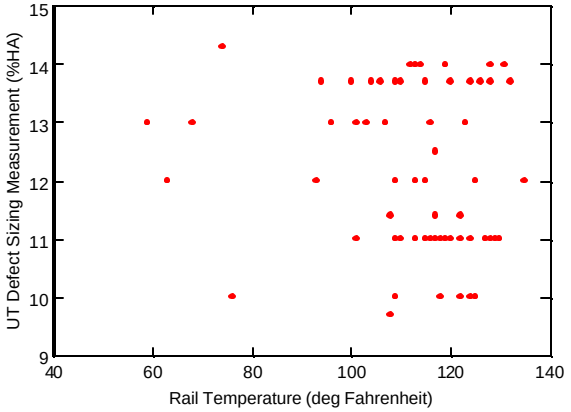

(d) Flaw D

Figure 6. Ultrasonic size measurement as a function of rail temperature for four defects.

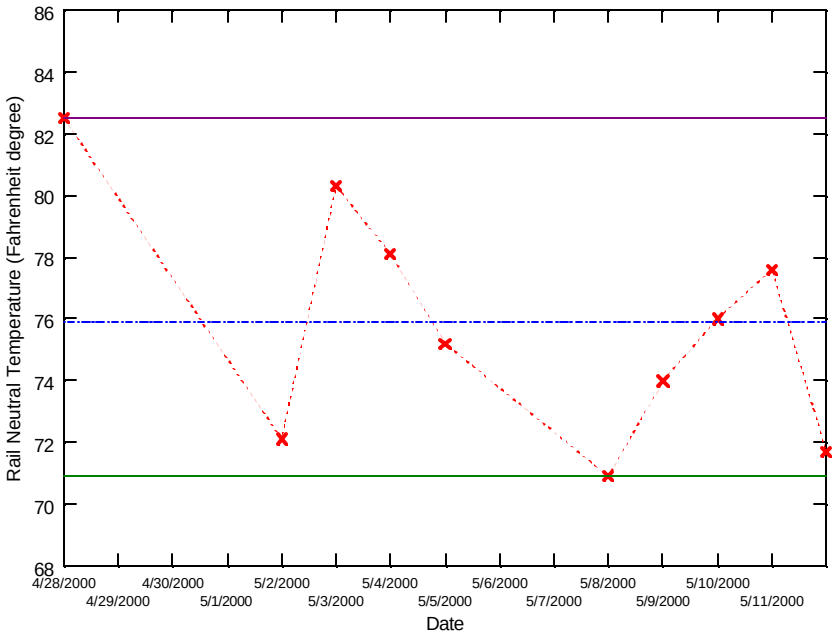

Figure 7. Variation of rail neutral temperature for FAST Flaw F1.

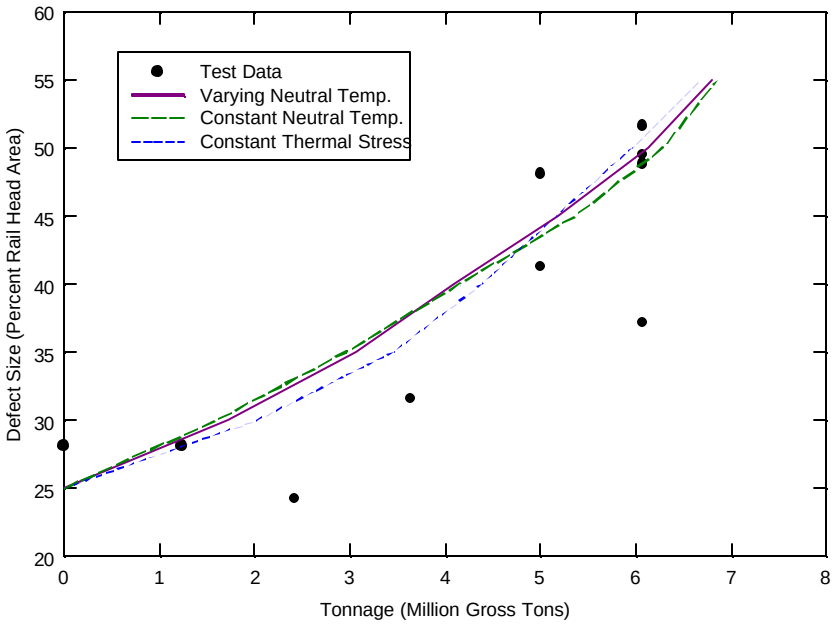

Figure 8. Effect of rail neutral temperature assumption on analysis of FAST Flaw F1.

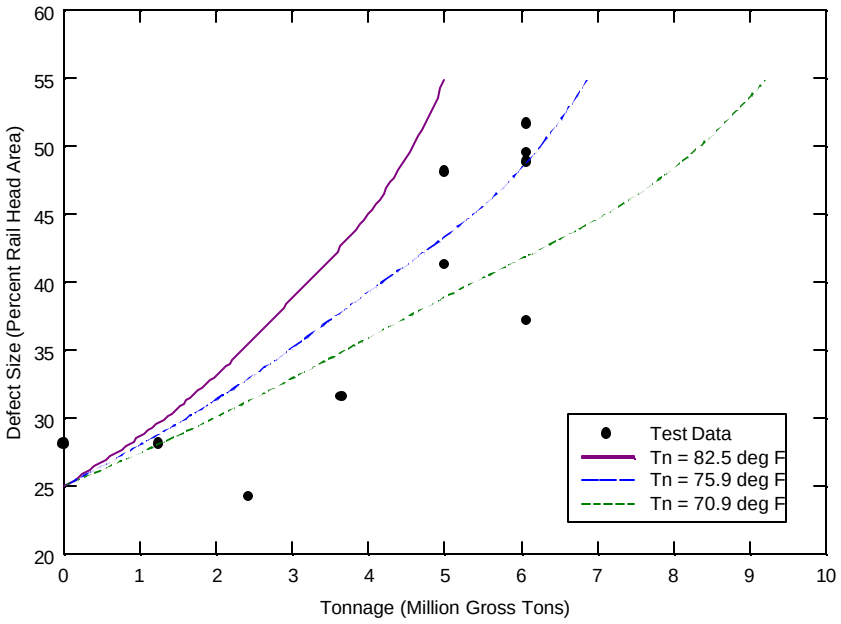

Figure 9. Effect of constant rail neutral temperature on analysis of FAST Flaw F1.

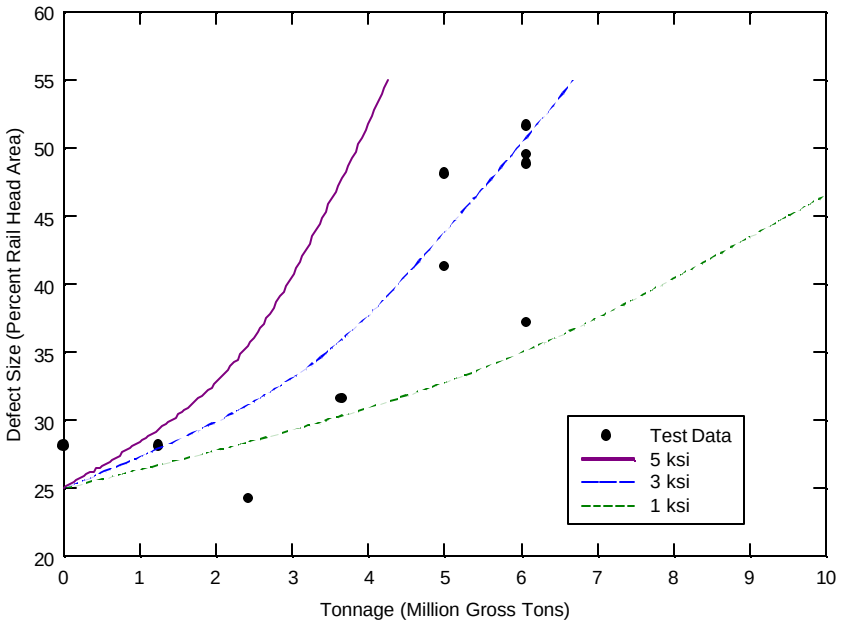

Figure 10. Effect of constant thermal stress on analysis of FAST Flaw F1.

Additional work is needed to complement the testing and analytical efforts described in this report. For example, the rails containing defects should be broken open to confirm the ultrasonic sizing measurements. Fractographic analysis may provide additional information on the fatigue-crack growth characteristics of these defects.

Measurements of the magnitude and distribution of the residual stresses, particularly in the rail head, are needed to validate the results of the engineering analyses. The most promising method for such purpose at this time is neutron diffraction (Gnäupel-Herold, et al., 1999). The cost of applying this method to measure residual stresses in all rail samples is prohibitive. Thus, a limited number of residual stress measurements using the neutron diffraction method will be conducted in the future.

The results presented in this report suggest that engineering analyses based on fracture mechanics principles can be applied to calculate realistic and consistent estimates of rail defect growth rates.

REFERENCES

Clayton, P., and Y.H. Tang, 1992: "Detail fracture growth in curved track at the Facility for Accelerated Service Testing," *Residual Stresses in Rails, Vol. 1,* Kluwer Academic Publishers, The Netherlands, 37-56.

Gnäupel-Herold, T., P.C. Brand, and H.J. Prask, 1999: "Neutron Diffraction Investigation of Residual Stresses in Transverse/Oblique Rail Slices Subjected to Different Grinding Strategies." National Institute of Standards and Technology Report: NISTIR 6305.

Jeong, D.Y., 2002: "Correlations Between Rail Defect Growth Test Data and Engineering Analyses, Part I: Laboratory Tests," Volpe Center Technical Report for the UIC/WEC Joint Research Project on Rail Defect Management.

Kish, A., G. Samavedam, and D. Jeong, 1987: "The neutral temperature variation of continuous welded rails," *American Railway Engineering Association Bulletin 712*, Vol. 88, 257-279.

Orringer, O., Y.H. Tang, J.E. Gordon, D.Y. Jeong, J.M. Morris, and A.B. Perlman, 1988: "Crack Propagation Life of Detail Fractures in Rails," Final Report, DOT/FRA/ORD-88/13.

Sih. G.C., 1973: *Handbook of Stress Intensity Factors*, Institute of Fracture and Solid Mechanics, Lehigh University, Bethlehem, PA.

Scutti, J.J., R.M. Pelloux, and R. Fuquen-Moleno, 1984: "Fatigue behavior of a rail steel," *Fatigue & Fracture of Engineering Materials & Structures 7*, 121-135.

APPENDIX A. SECTION PROPERTIES FOR RAIL SAMPLES

			UIC 60	132 RE	133RE	136RE
Area Moments of Inertia	I_{yy}	vertical bending inertia for entire rail	3055 cm^4 (73.4 in^4)	3671 cm^4 (88.2 in^4)	3592 cm^4 (86.3 in^4)	3950 cm^4 (94.9 in^4)
	I_{zz}	lateral bending inertia for entire rail	507.8 cm^4 (12.2 in^4)	591.0 cm^4 (14.2 in^4)	622.3 cm^4 (15.0 in^4)	603.5 cm^4 (14.5 in^4)
	I_{yyH}*	vertical bending inertia for rail head only	49.50 cm^4 (1.19 in^4)	34.84 cm^4 (0.837 in^4)	45.79 cm^4 (1.10 in^4)	48.70 cm^4 (1.17 in^4)
	I_{zzH}*	lateral bending inertia for rail head only	119.0 cm^4 (2.86 in^4)	118.2 cm^4 (2.84 in^4)	118.6 cm^4 (2.85 in^4)	126.1 cm^4 (3.03 in^4)
	I_{yyzB}*	vertical bending inertia for rail base only	14.7 cm^4 (0.35 in^4)	15.7 cm^4 (0.38 in^4)	18.3 cm^4 (0.44 in^4)	15.7 cm^4 (0.38 in^4)
	I_{zzB}*	lateral bending inertia for rail base only	382.9 cm^4 (9.2 in^4)	462.0 cm^4 (11.1 in^4)	489.1 cm^4 (11.8 in^4)	466.2 cm^4 (11.2 in^4)
Cross-Sectional Areas	A_R	cross-sectional area of entire rail	76.86 cm^2 (11.91 in^2)	83.55 cm^2 (12.95 in^2)	84.52 cm^2 (13.10 in^2)	86.13 cm^2 (13.35 in^2)
	A_H*	cross-sectional area of rail head only	30.92 cm^2 (4.79 in^2)	28.52 cm^2 (4.42 in^2)	30.32 cm^2 (4.70 in^2)	31.35 cm^2 (4.86 in^2)
	A_B*	cross-sectional area of rail base only	28.42 cm^2 (4.40 in^2)	31.35 cm^2 (4.86 in^2)	32.77 cm^2 (5.08 in^2)	31.42 cm^2 (4.87 in^2)
Rail Dimensions	h_{tot}	total rail height	17.2 cm (6.772 in)	18.1 cm (7.125 in)	17.9 cm (7.063 in)	18.6 cm (7.313 in)
	h_N	height of rail neutral axis	8.10 cm (3.189in)	8.13 cm (3.201in)	8.13 cm (3.200 in)	8.51 cm (3.351 in)
	h_{NH}	height of neutral axis of rail head only	14.87 cm (5.85 in)	16.00 cm (6.30 in)	15.62 cm (6.15 in)	16.23 cm (6.39 in)
	h_{NB}	height of neutral axis of rail base only	1.06 cm (0.42 in)	1.10 cm (0.44 in)	1.14 cm (0.45 in)	1.10 cm (0.44 in)
	h_w	rail web height	8.95 cm (3.52 in)	10.64 cm (4.19 in)	10.00 cm (3.938 in)	10.56 cm (4.156 in)
	t_w	rail web thickness	1.65 cm (0.65 in)	1.67 cm (0.66 in)	1.75 cm (0.69 in)	1.75 cm (0.69 in)
	w_H	rail head width	7.43 cm (2.92 in)	7.62 cm (3.00 in)	7.62 cm (3.00 in)	7.46 cm (2.94 in)
	w_B	rail base width	15.0 cm (5.91 in)	15.2 cm (6.00 in)	15.2 cm (6.00 in)	15.9 cm (6.25 in)

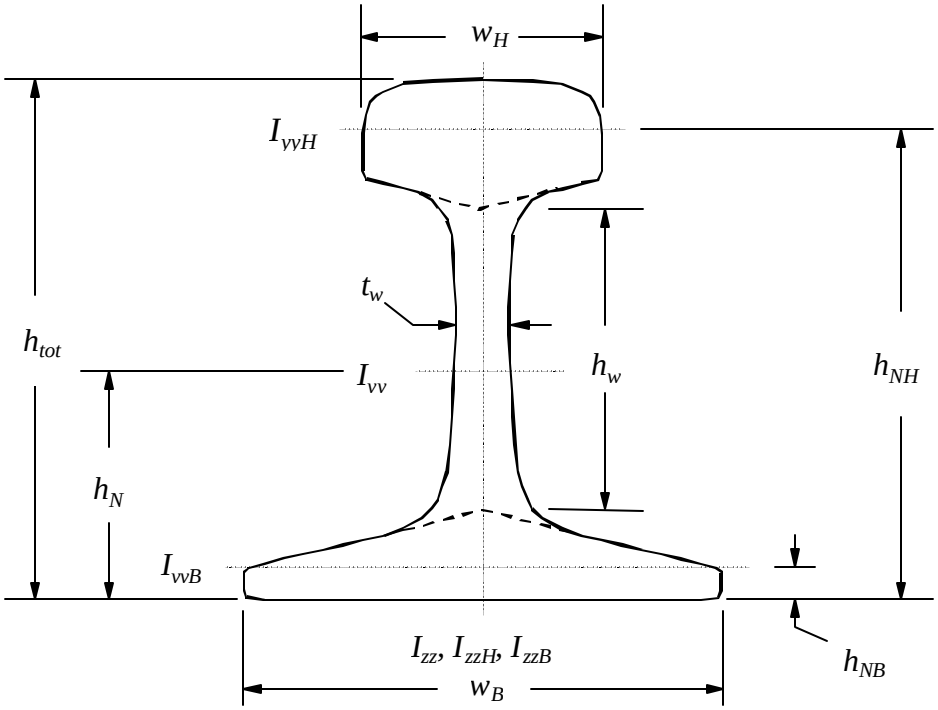

Figure A.1 Definitions of rail section properties.

APPENDIX B. CORRELATIONS BETWEEN FAST GROWTH TEST DATA AND RESULTS FROM ENGINEERING MODEL

This appendix contains 20 plots showing the growth rate of rail defects in the FAST test program. Defect size is given in percent rail head area (%HA). Tonnage expressed in million gross tons (MGT). These plots also show a comparison with calculations from the engineering fracture mechanics based model for rail defect growth. In each plot, solid diamond-shaped symbols represent the FAST test data and a solid continuous line represents the results from the analysis.

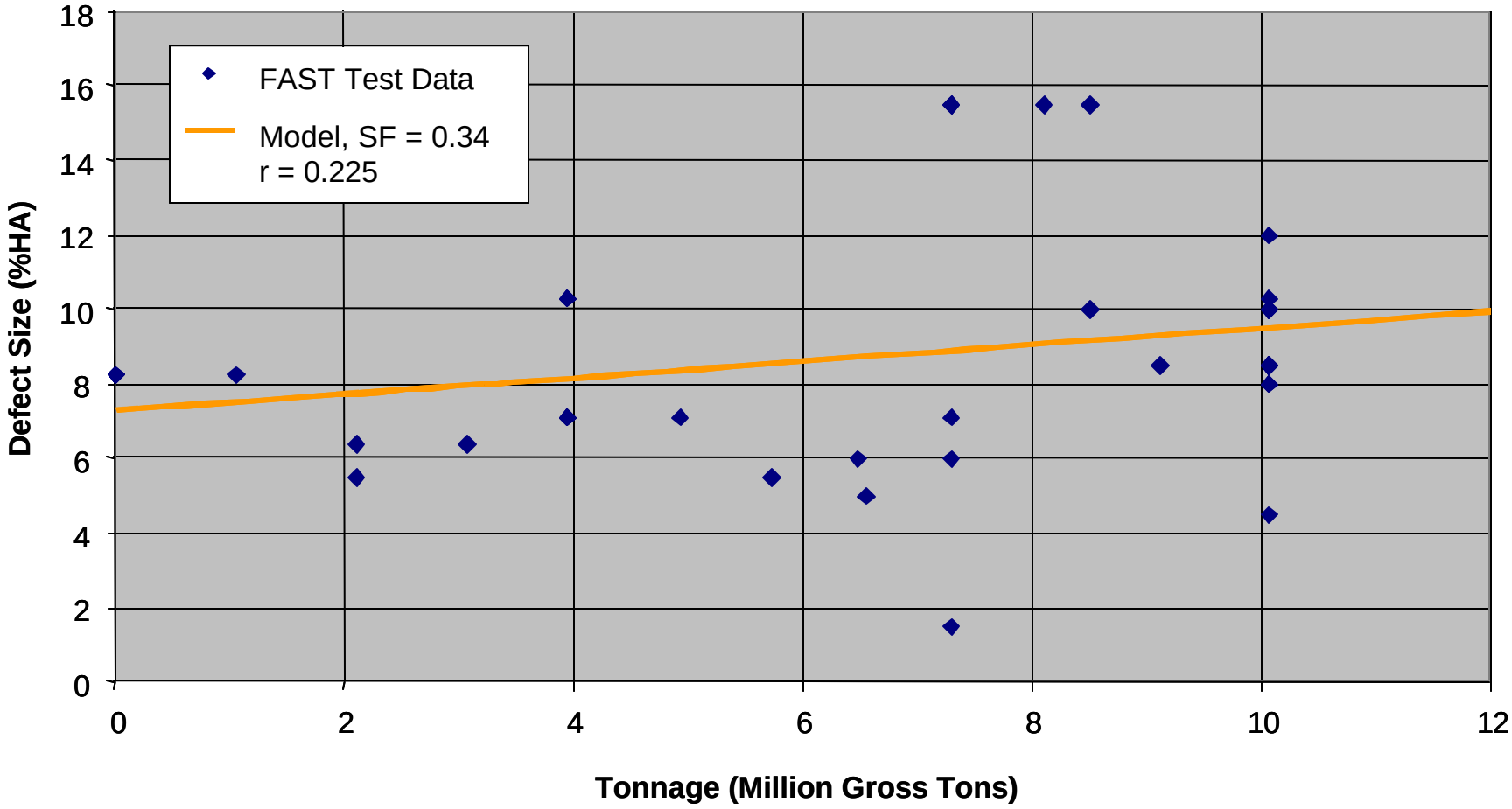

Figure B-1. Correlation between model results and FAST test data for Flaw 2A.

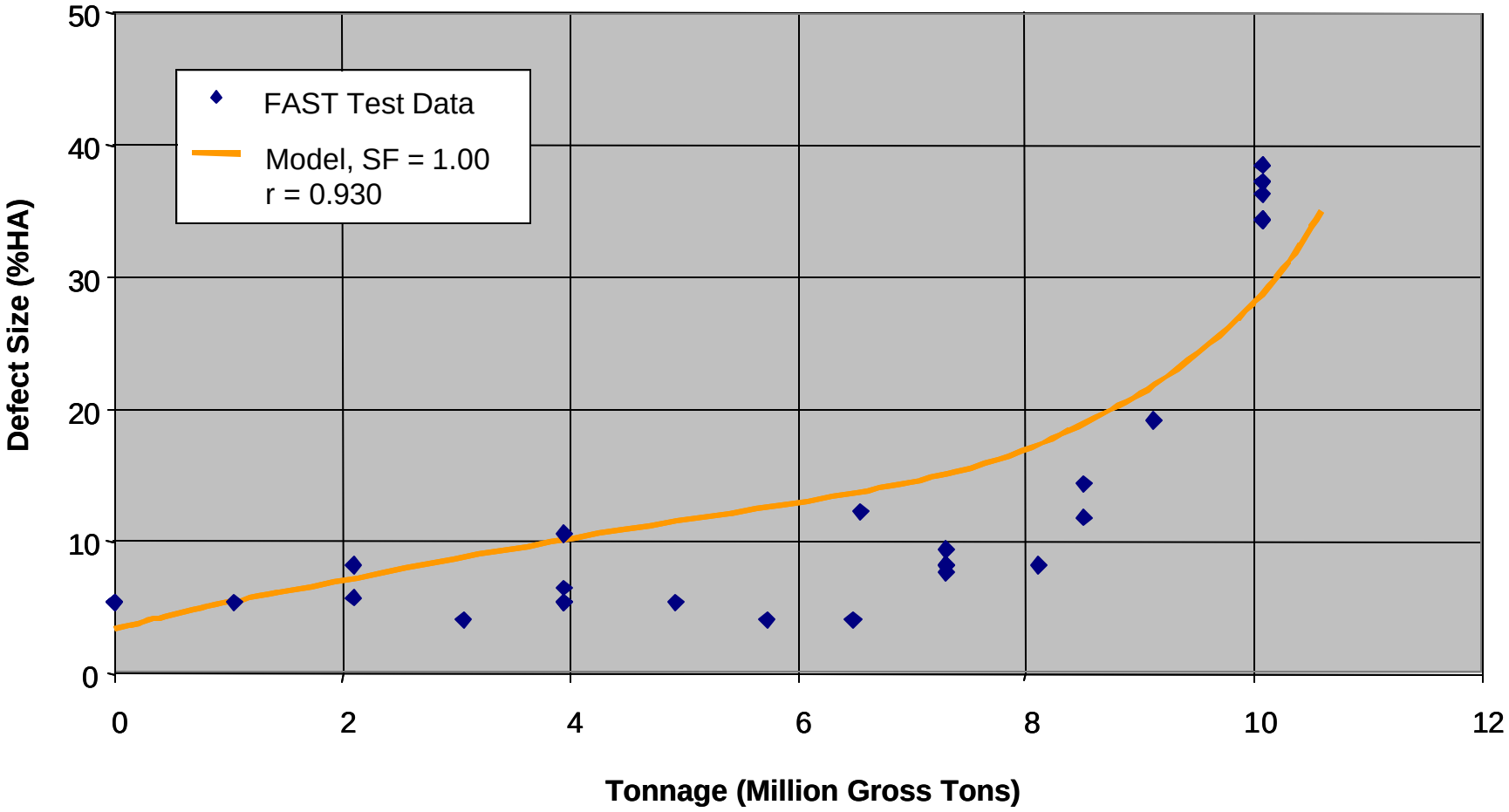

Figure B-2. Correlation between model results and FAST test data for Flaw 2B.

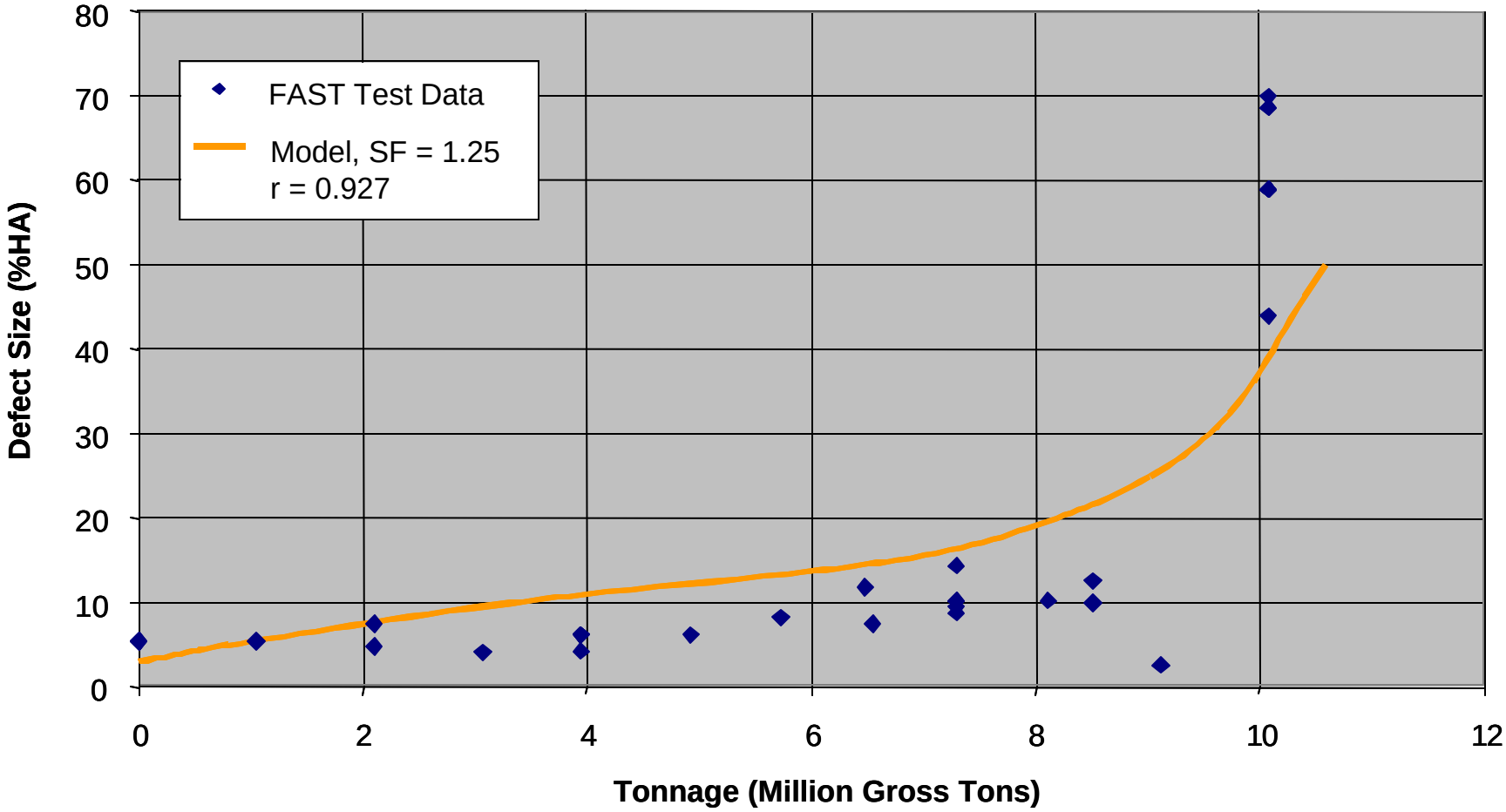

Figure B-3. Correlation between model results and FAST test data for Flaw 2C.

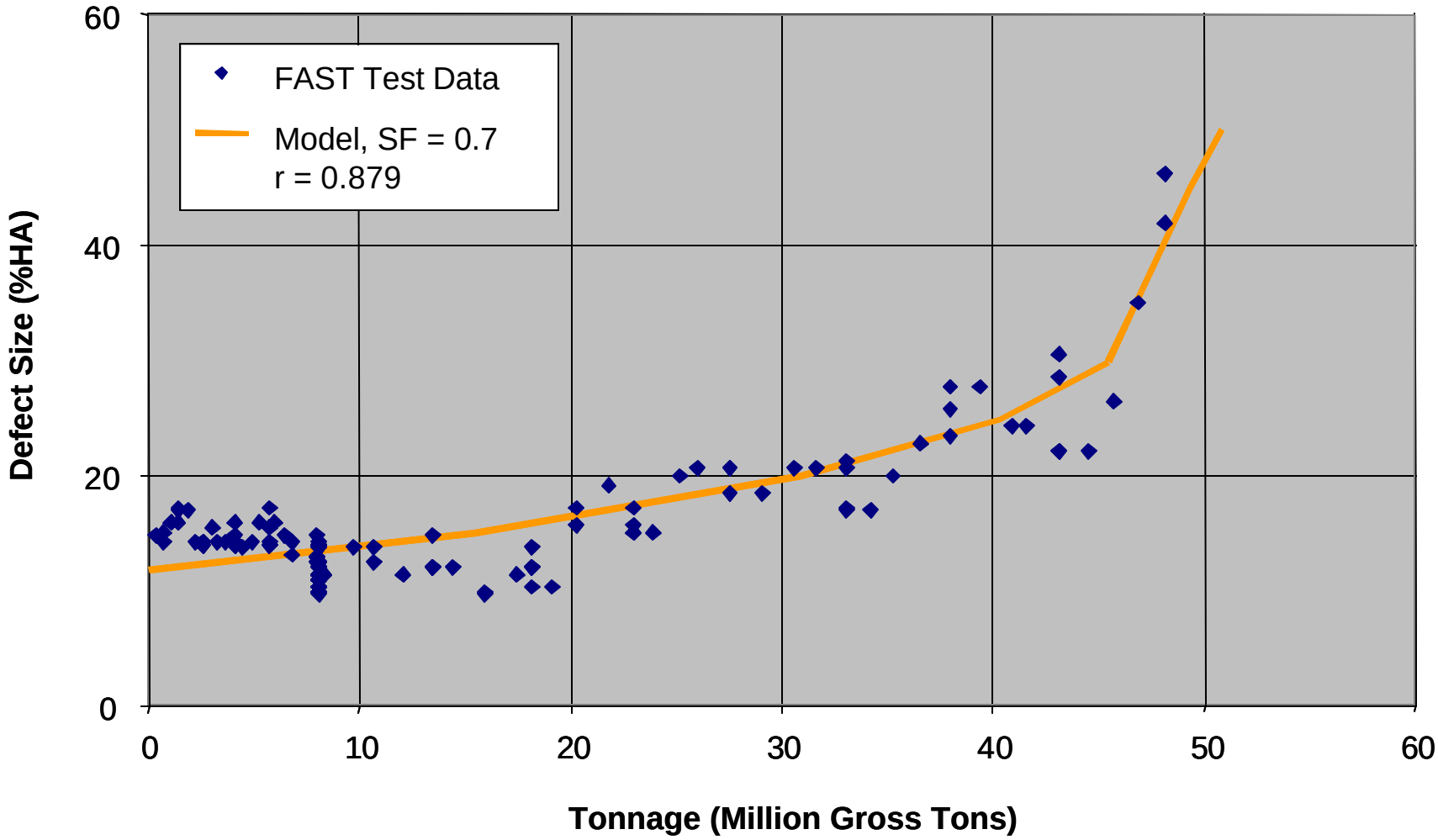

Figure B-4. Correlation between model results and FAST test data for Flaw 5.

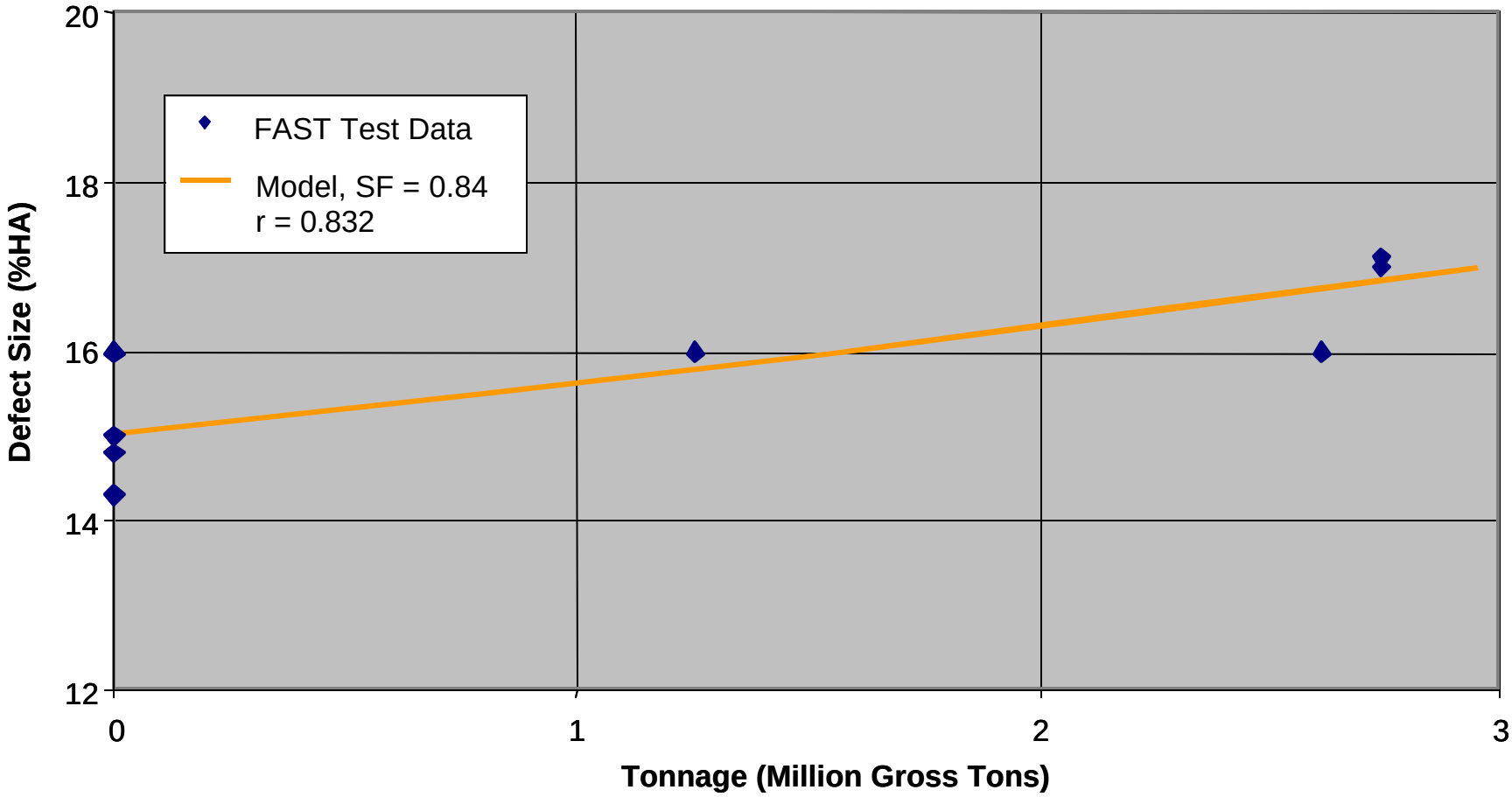

Figure B-5. Correlation between model results and FAST test data for Flaw D.

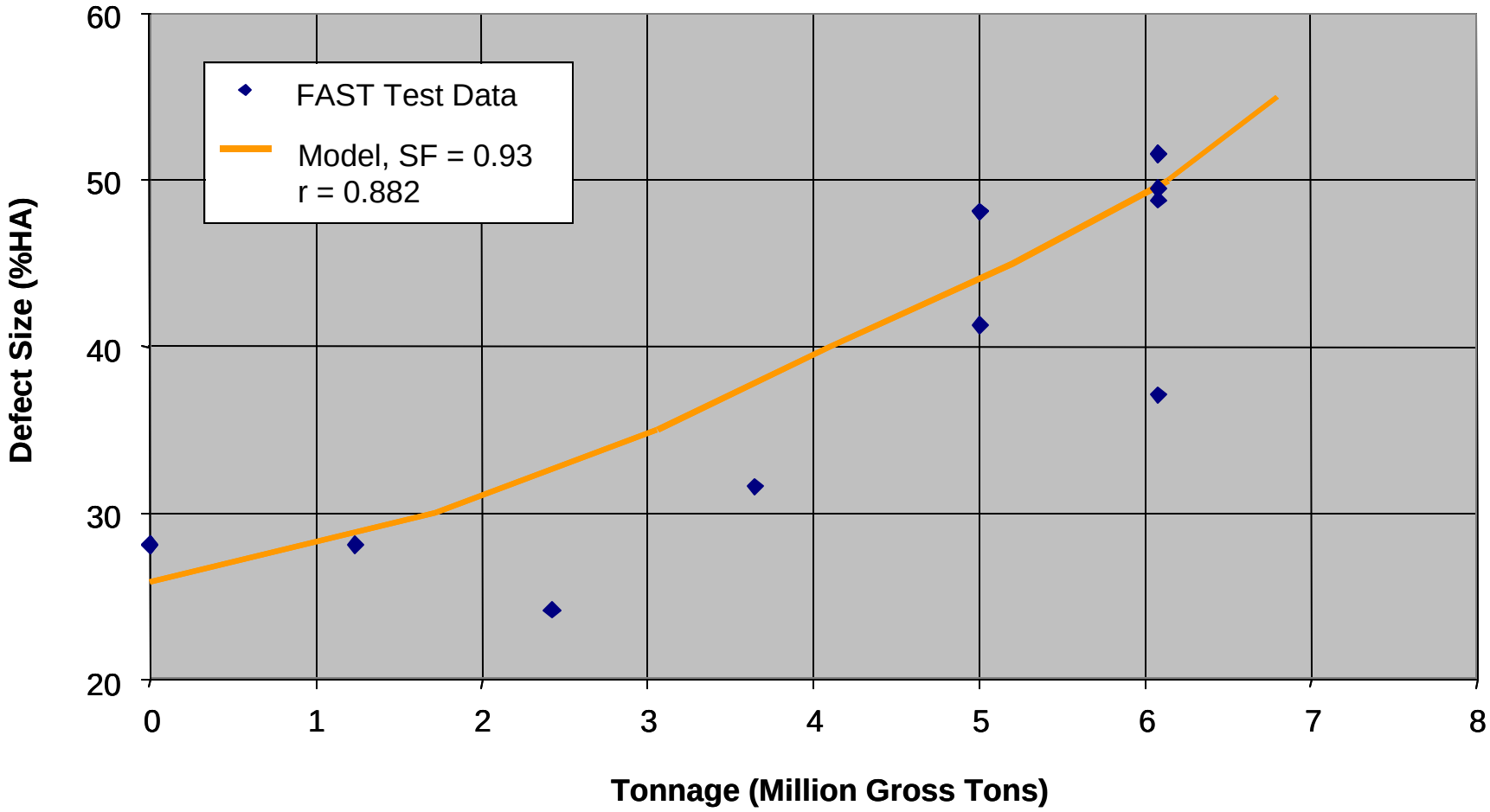

Figure B-6. Correlation between model results and FAST test data for Flaw F1.

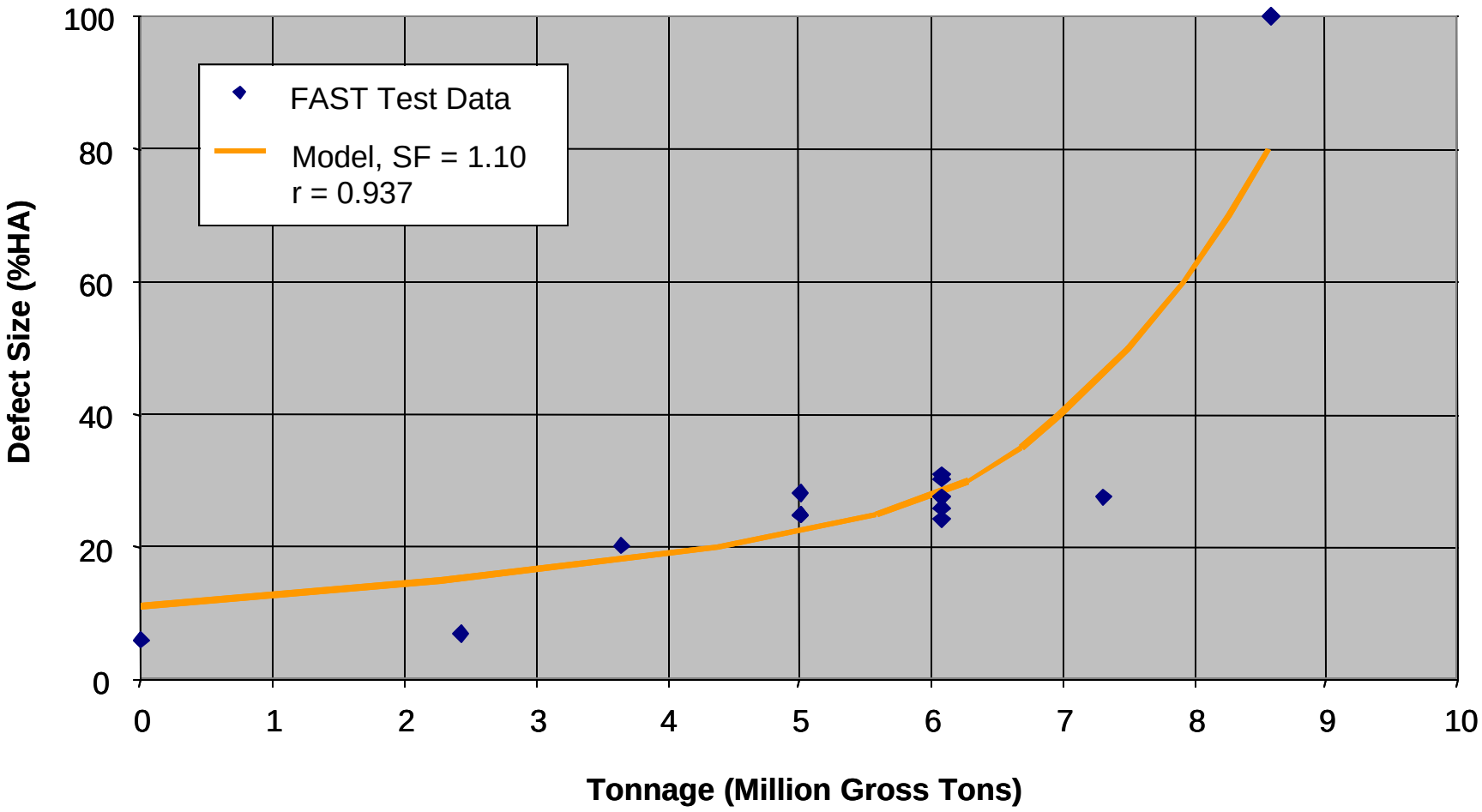

Figure B-7. Correlation between model results and FAST test data for Flaw F3.

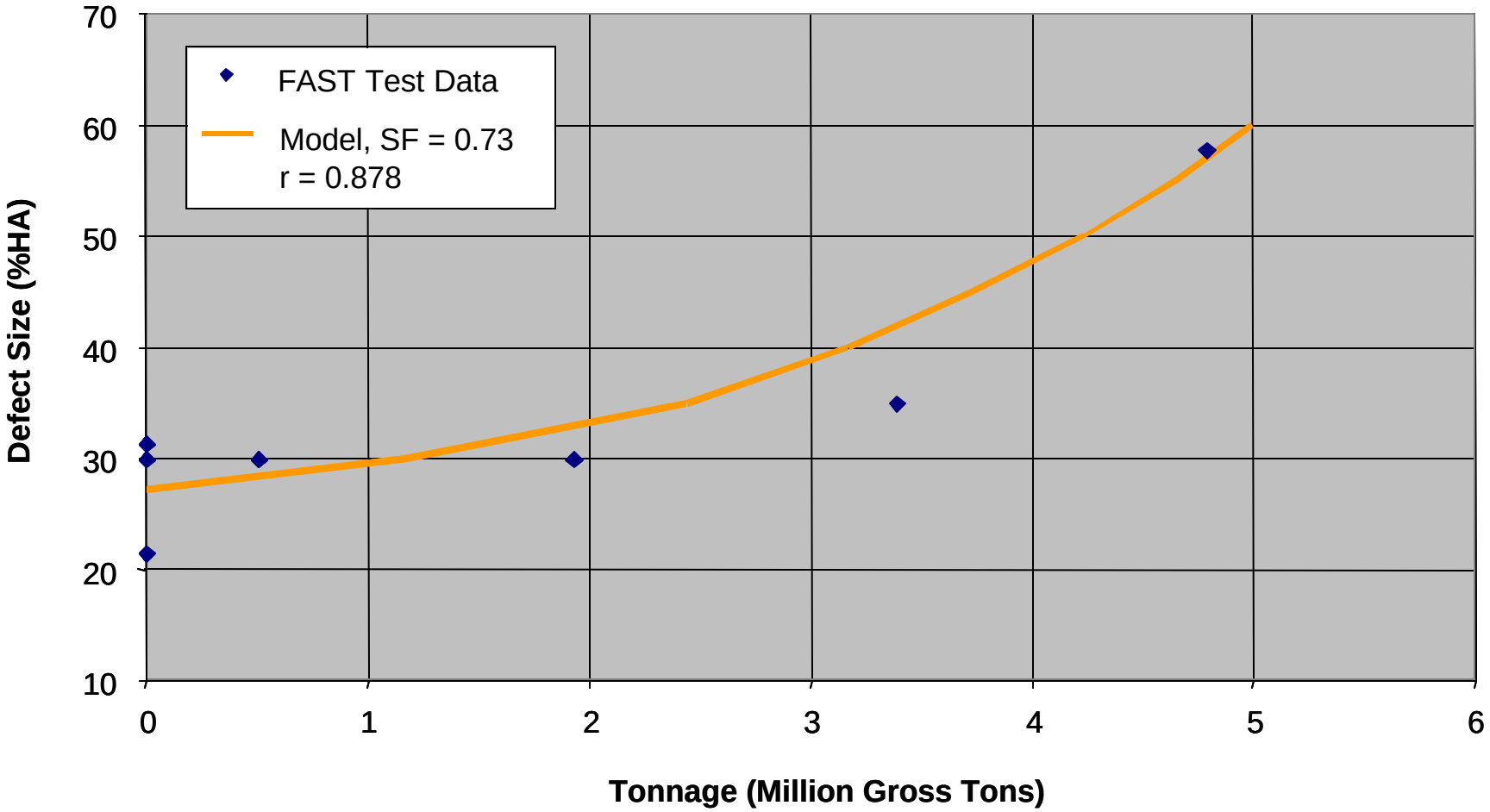

Figure B-8. Correlation between model results and FAST test data for Flaw F5.

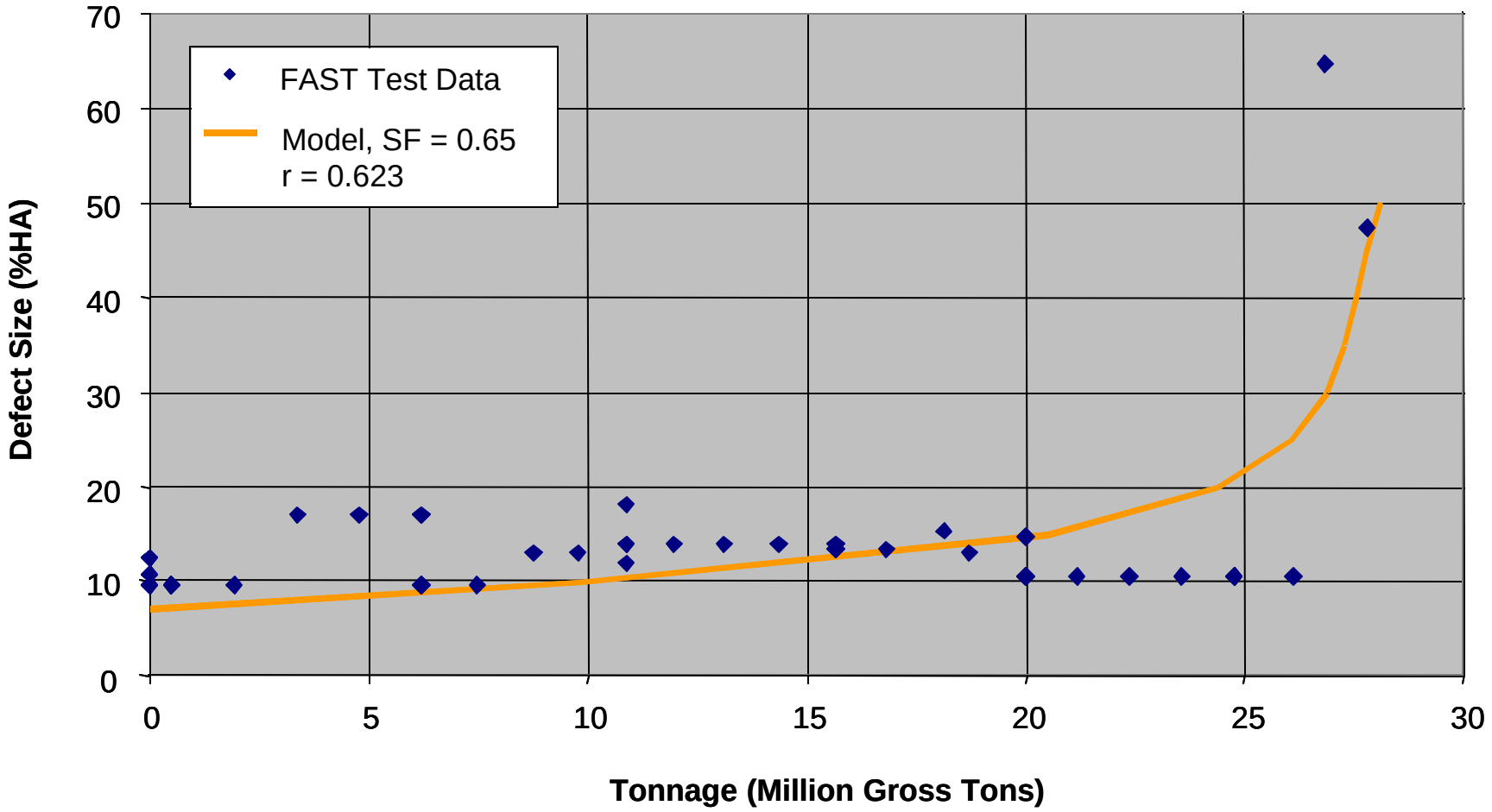

Figure B-9. Correlation between model results and FAST test data for Flaw F7.

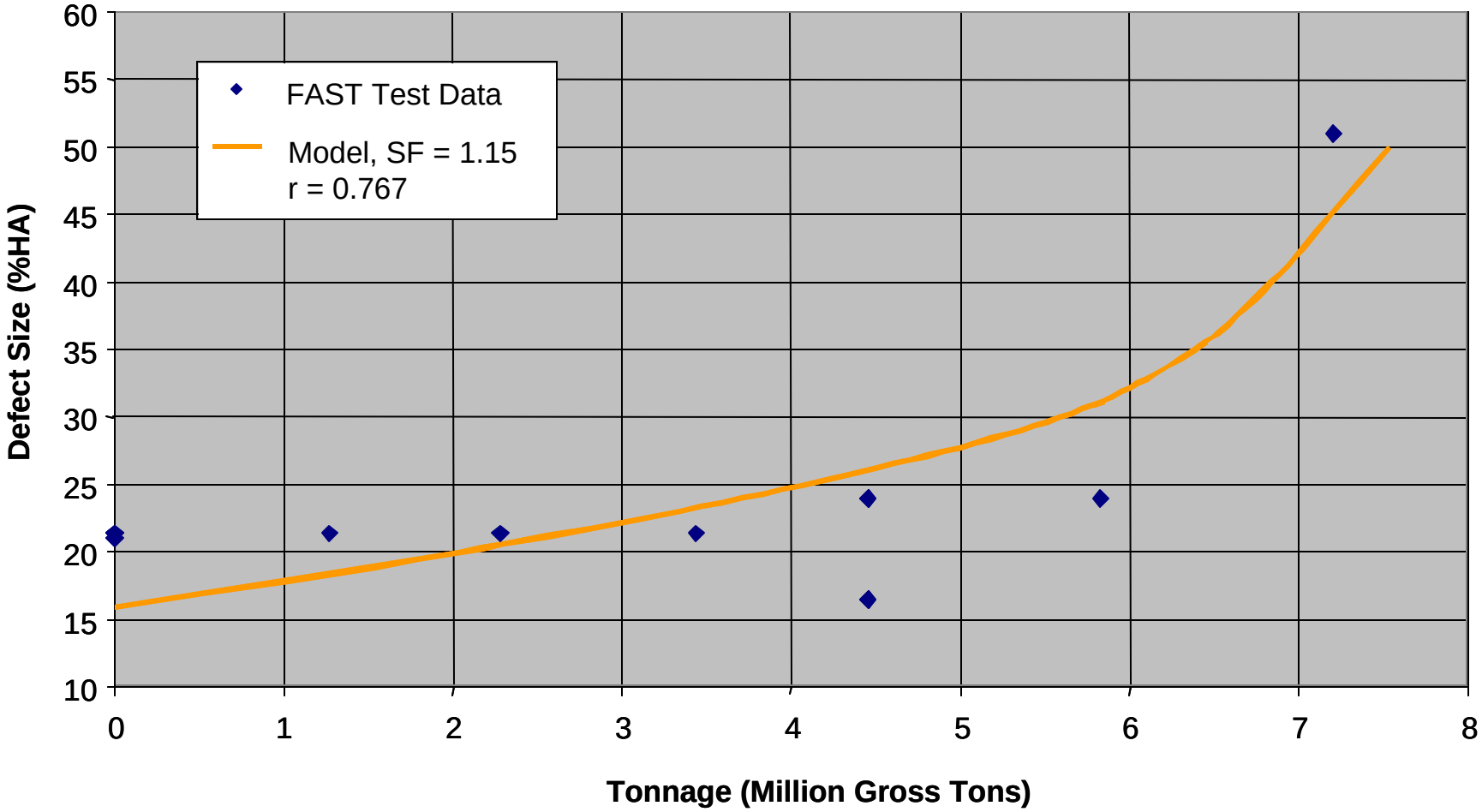

Figure B-10. Correlation between model results and FAST test data for Flaw F9.

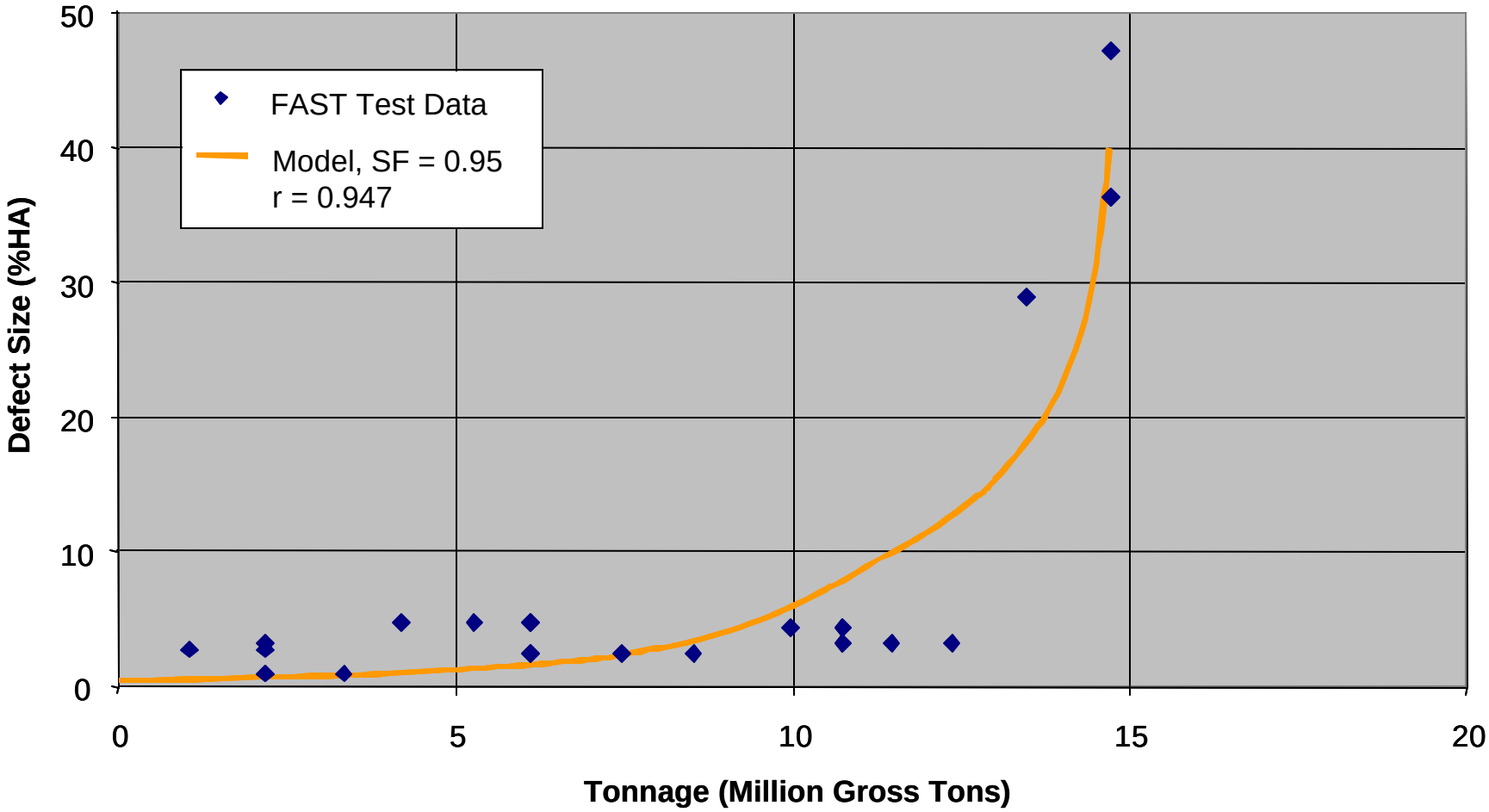

Figure B-11. Correlation between model results and FAST test data for Flaw B.

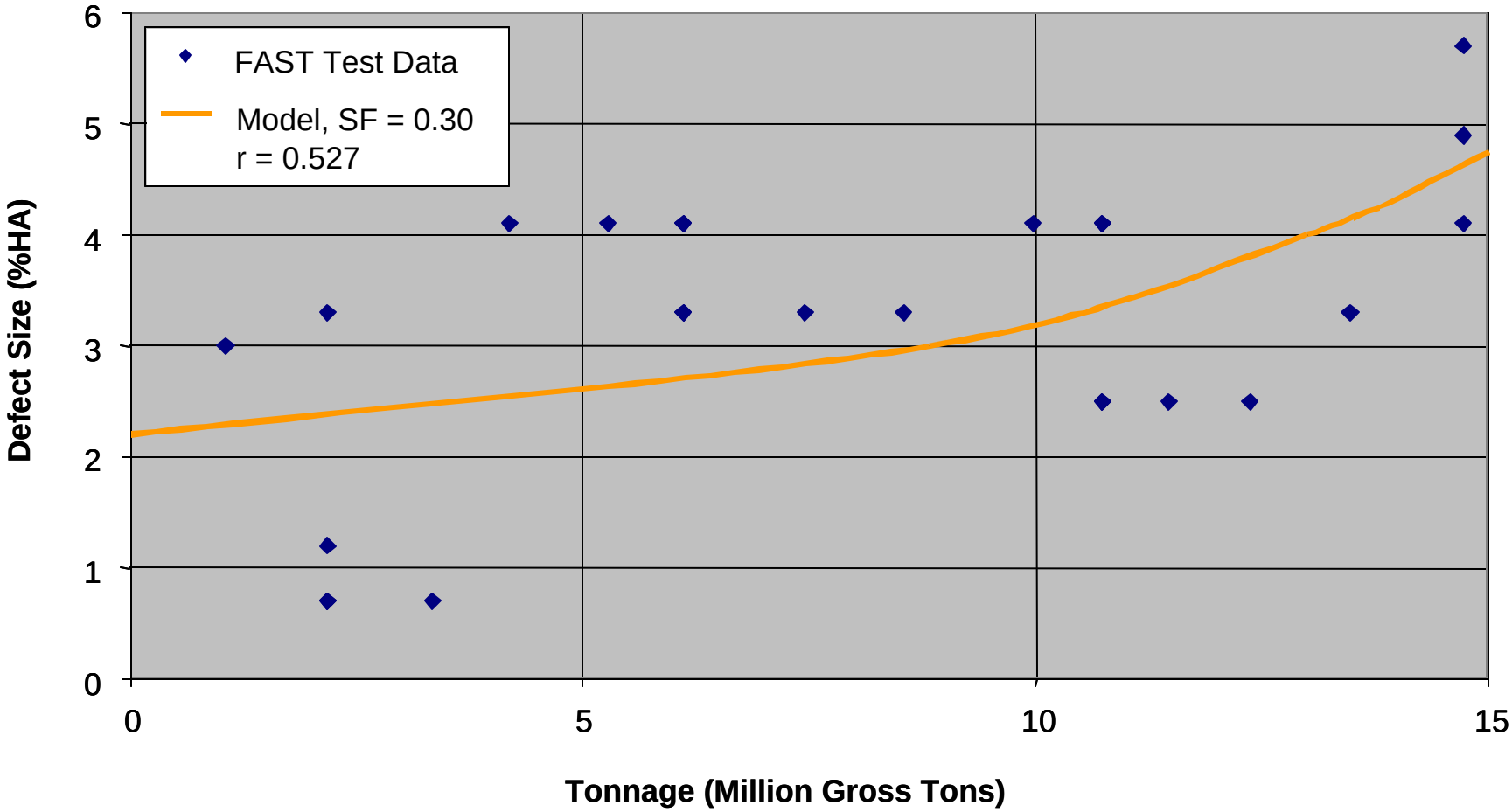

Figure B-12. Correlation between model results and FAST test data for Flaw C.

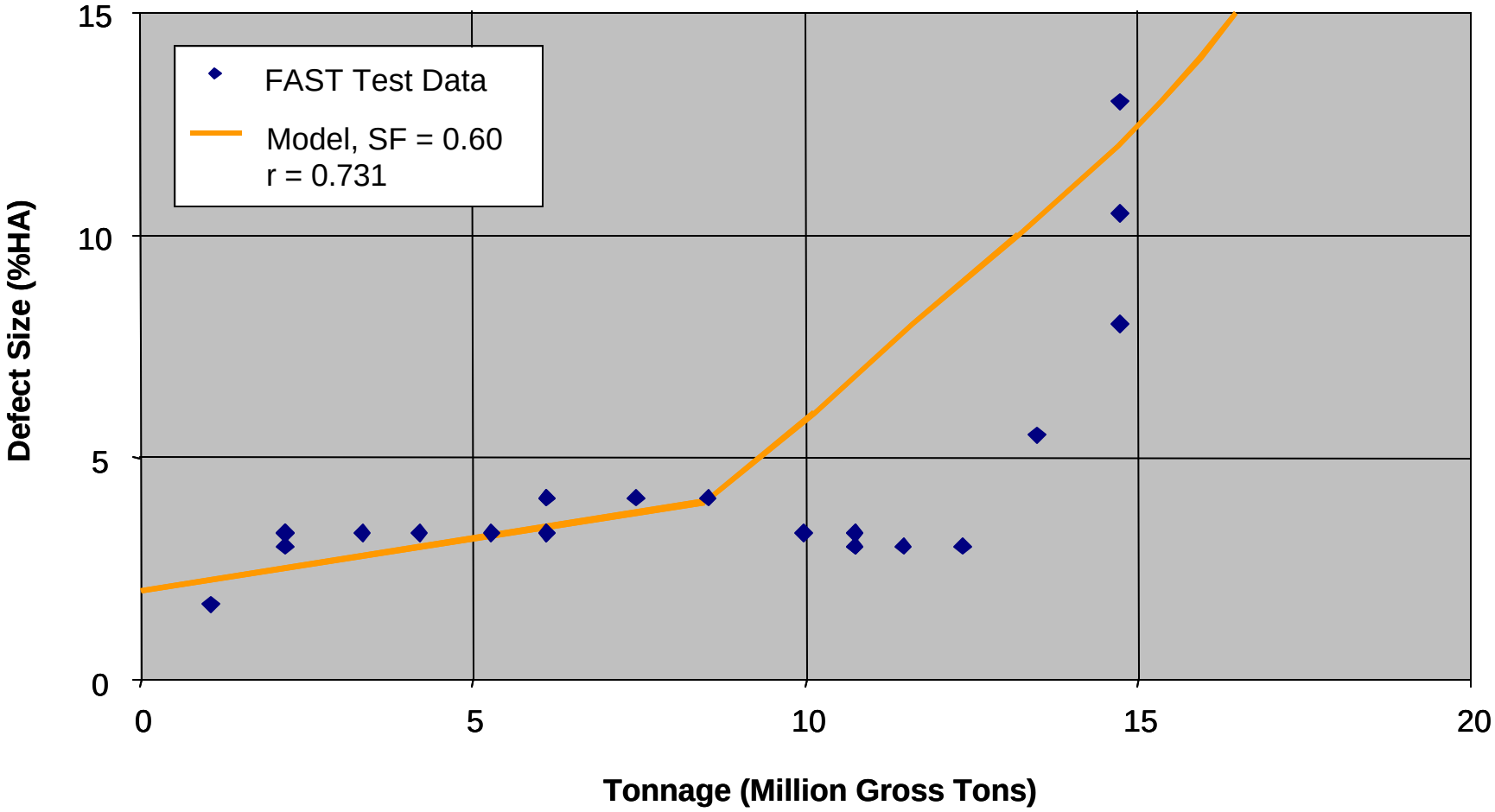

Figure B-13 Correlation between model results and FAST test data for Flaw E.

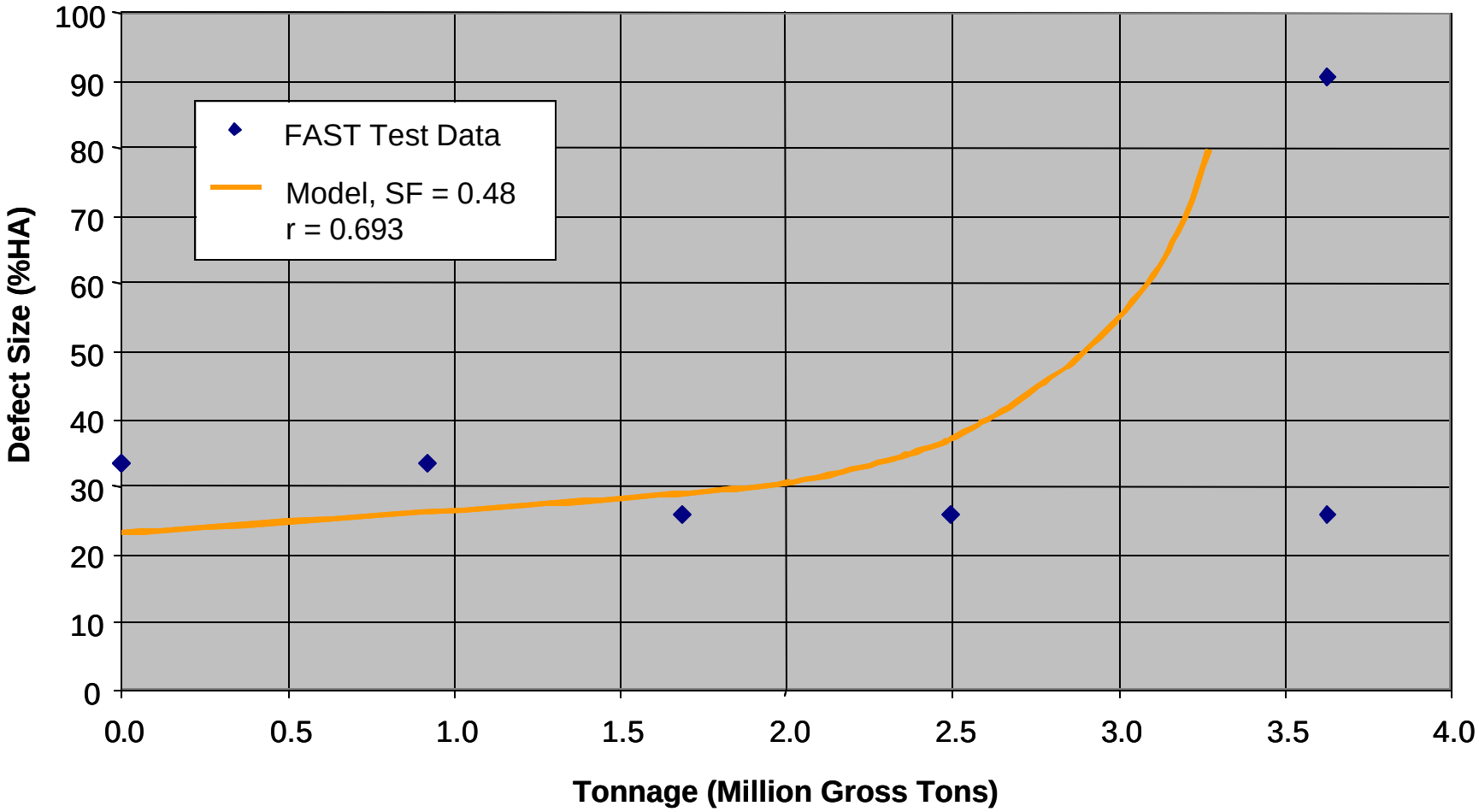

Figure B-14. Correlation between model results and FAST test data for Flaw J.

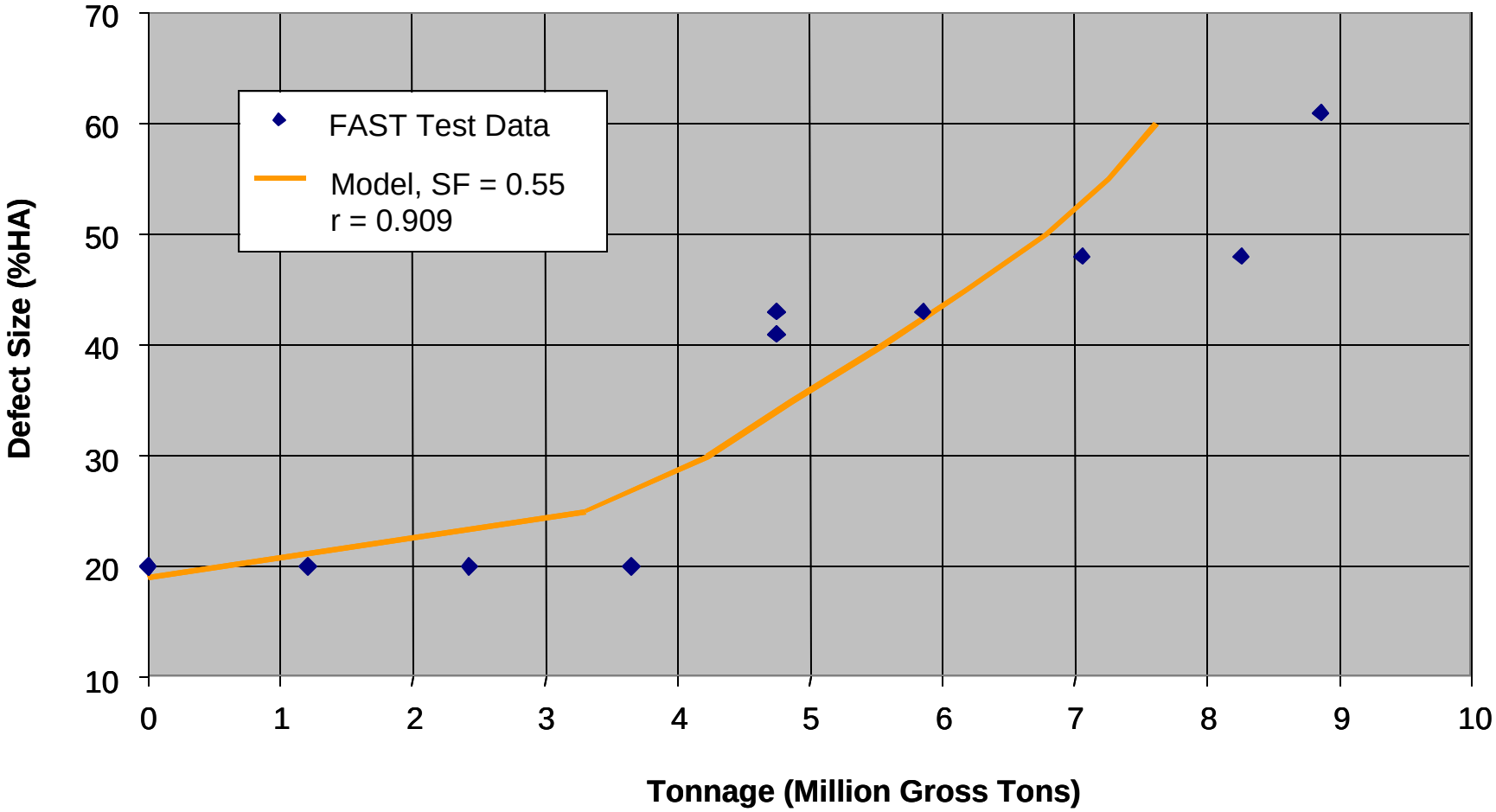

Figure B-15. Correlation between model results and FAST test data for Flaw K.

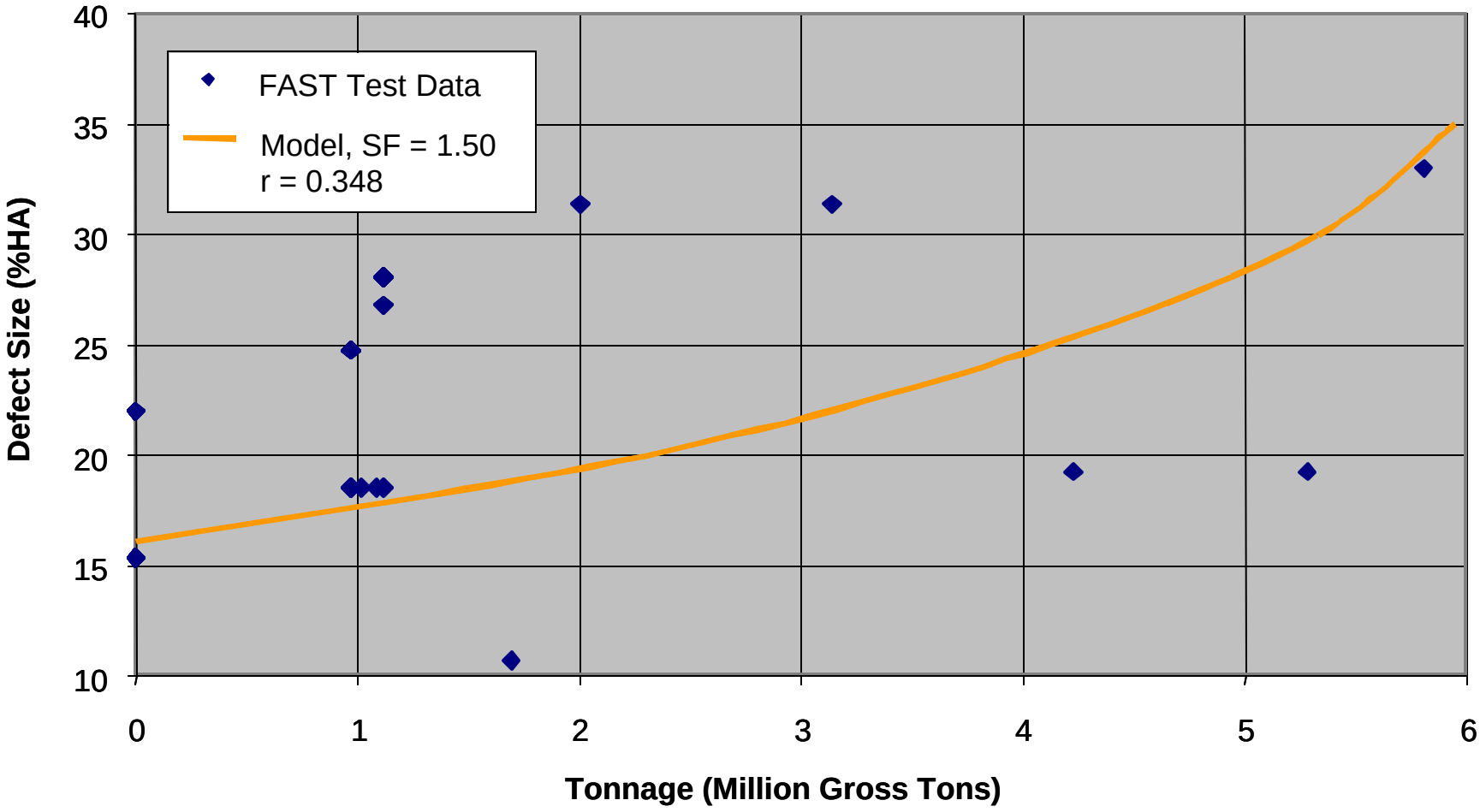

Figure B-16. Correlation between model results and FAST test data for Flaw GT12.

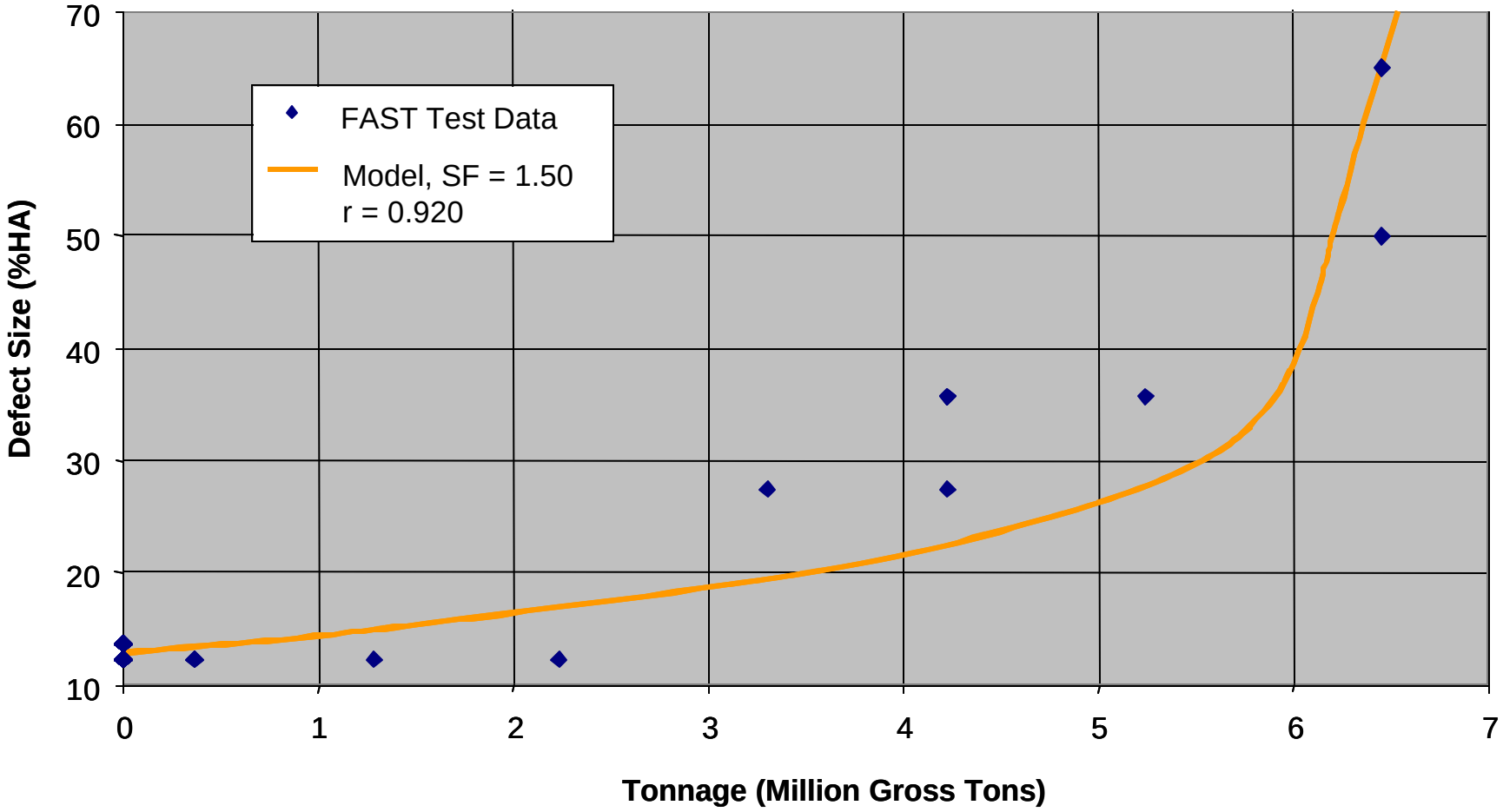

Figure B-17. Correlation between model results and FAST test data for Flaw F11.

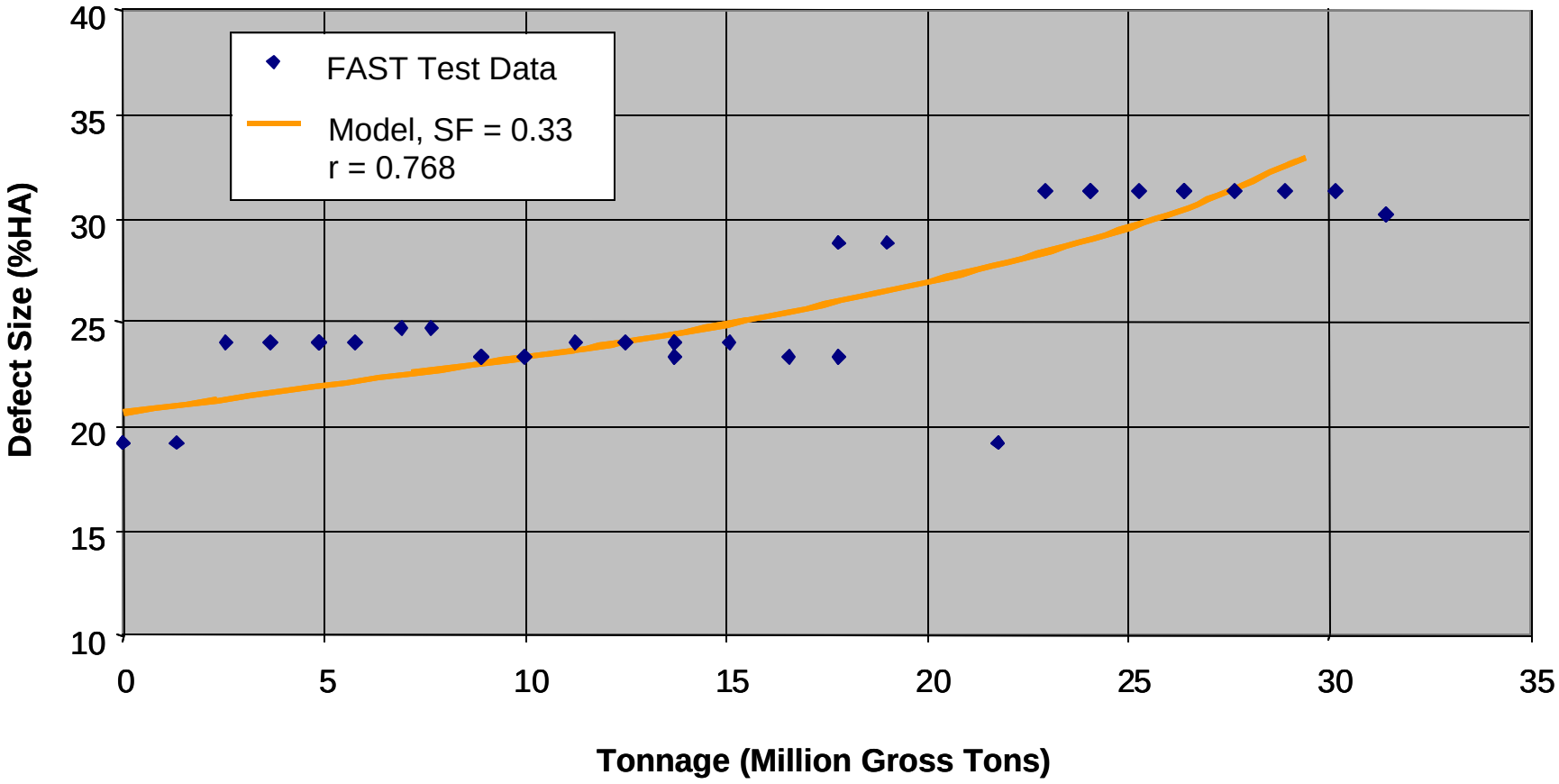

Figure B-18. Correlation between model results and FAST test data for Flaw Q.

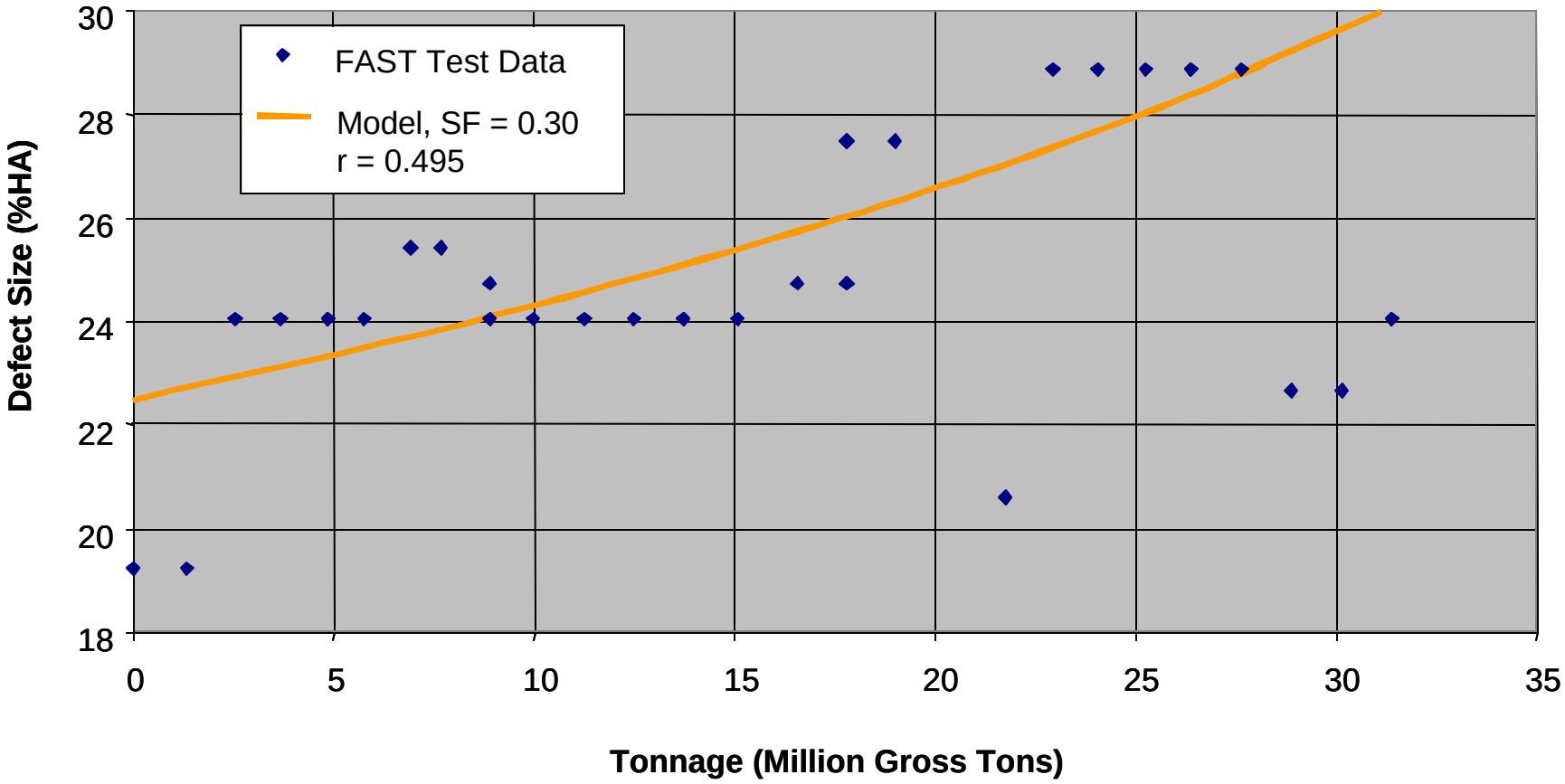

Figure B-19. Correlation between model results and FAST test data for Flaw R.

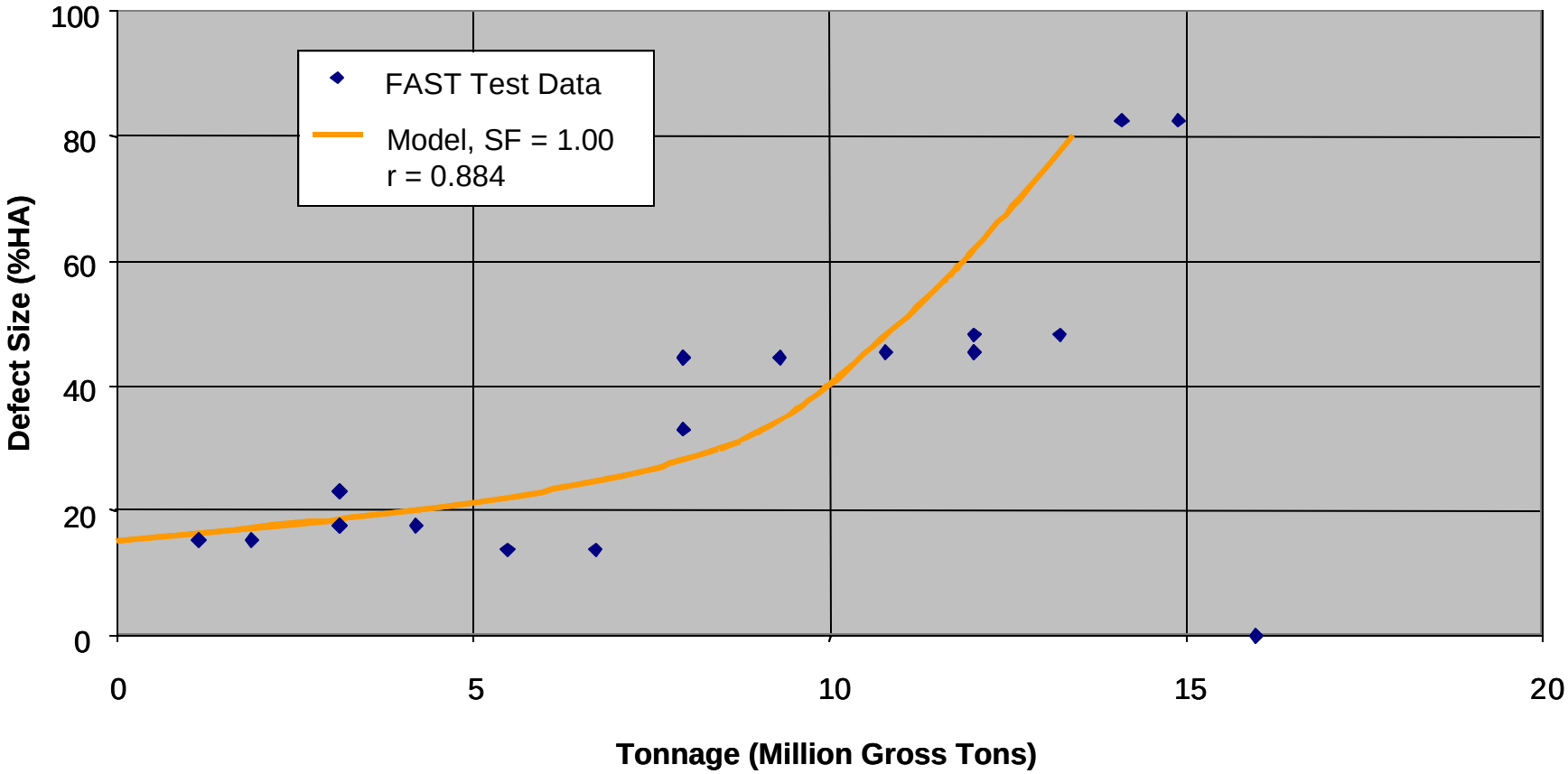

Figure B-20. Correlation between model results and FAST test data for Flaw S.

APPENDIX C. CORRELATIONS BETWEEN SPOORNET GROWTH TEST DATA AND RESULTS FROM ENGINEERING MODEL

This appendix contains seven plots showing the growth rate of rail defects from the Spoornet field test program. In these plots, the abscissa is expressed in terms of cycles and the ordinate is the defect size in millimeters (mm). Moreover, these plots compare the field test data with the growth rates calculated from the engineering fracture mechanics model. In each plot, the symbols represent the Spoornet field test data and a solid continuous line represents the results from the analysis.

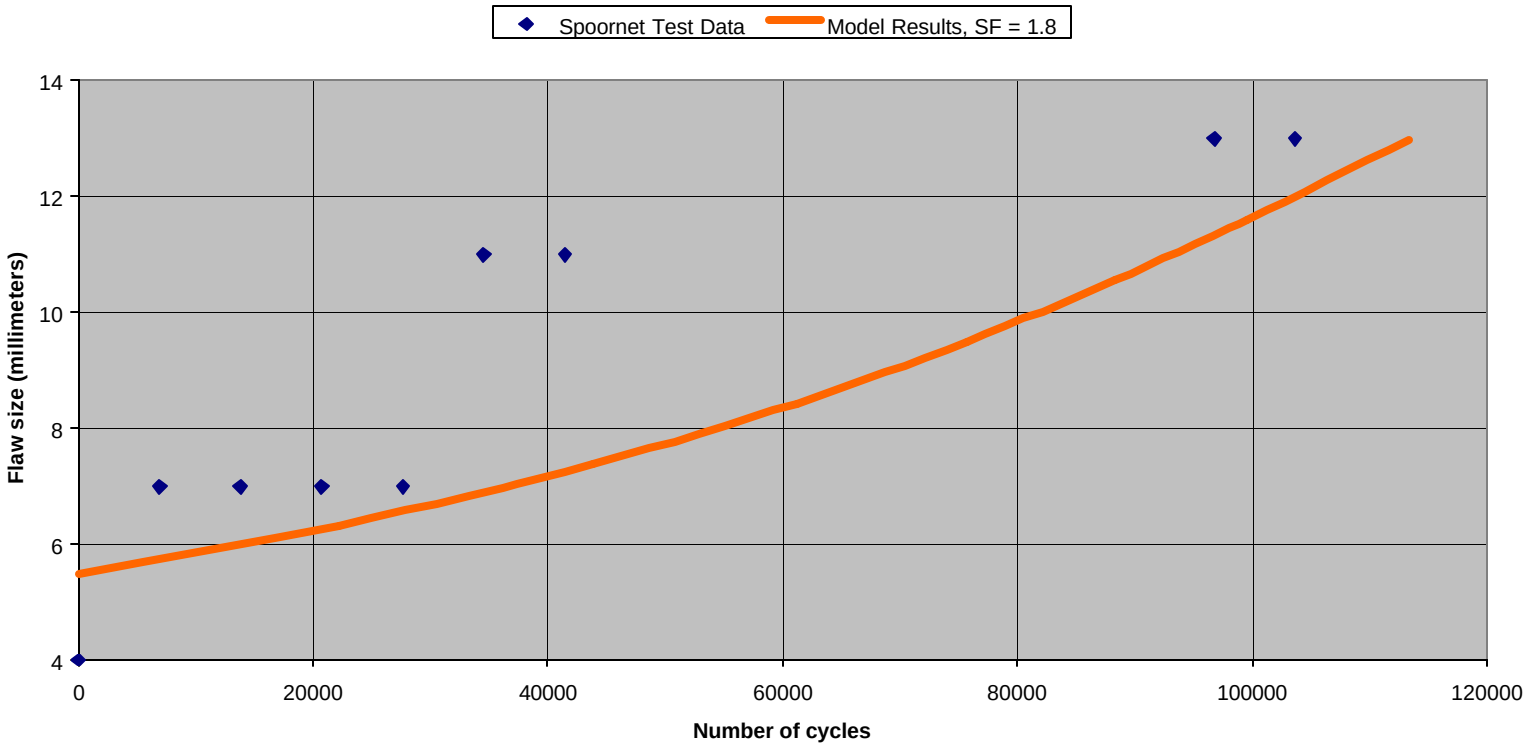

Figure C-1. Correlation between model results and Spoornet field test data for Defect No. 1432.

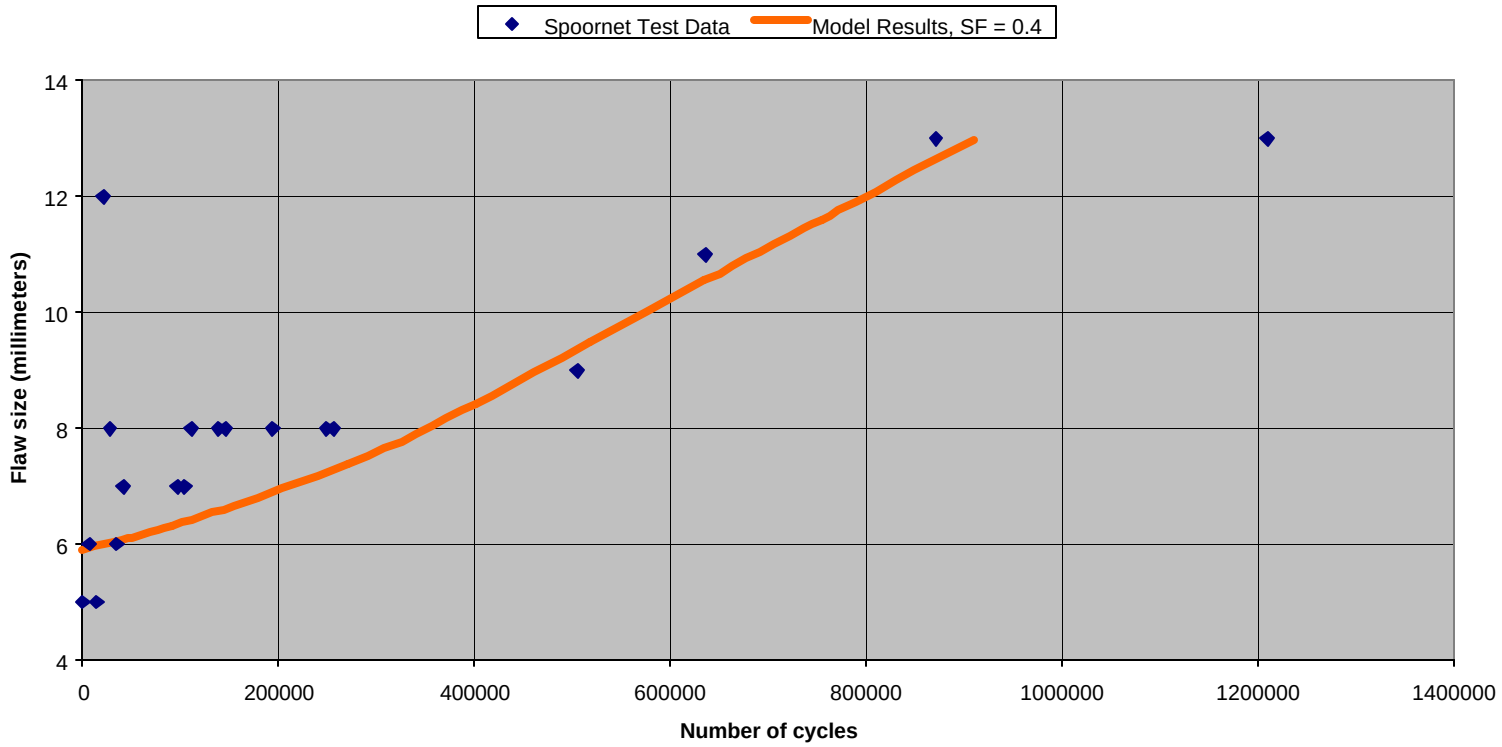

Figure C-2. Correlation between model results and Spoornet field test data for Defect No. 1435.

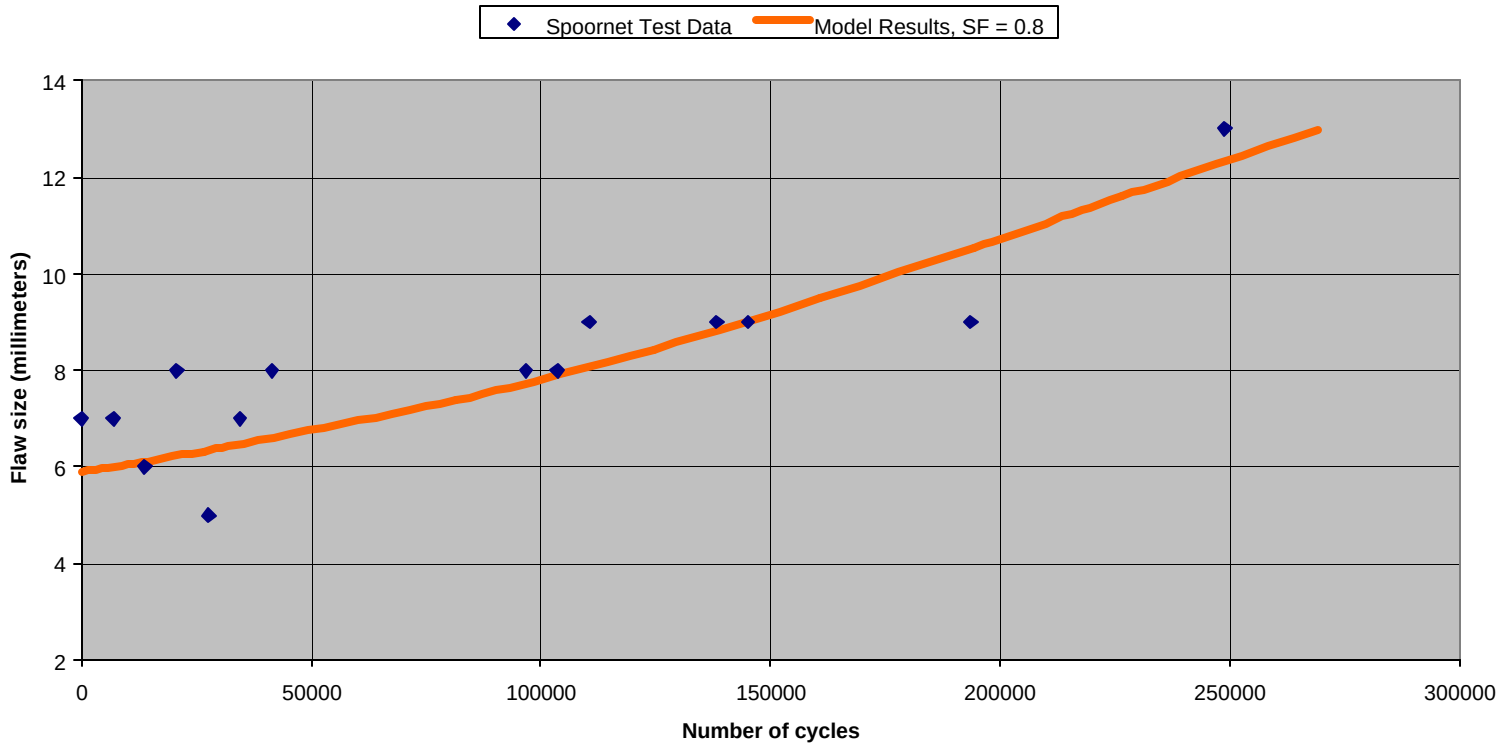

Figure C-3. Correlation between model results and Spoornet field test data for Defect No. 1454.

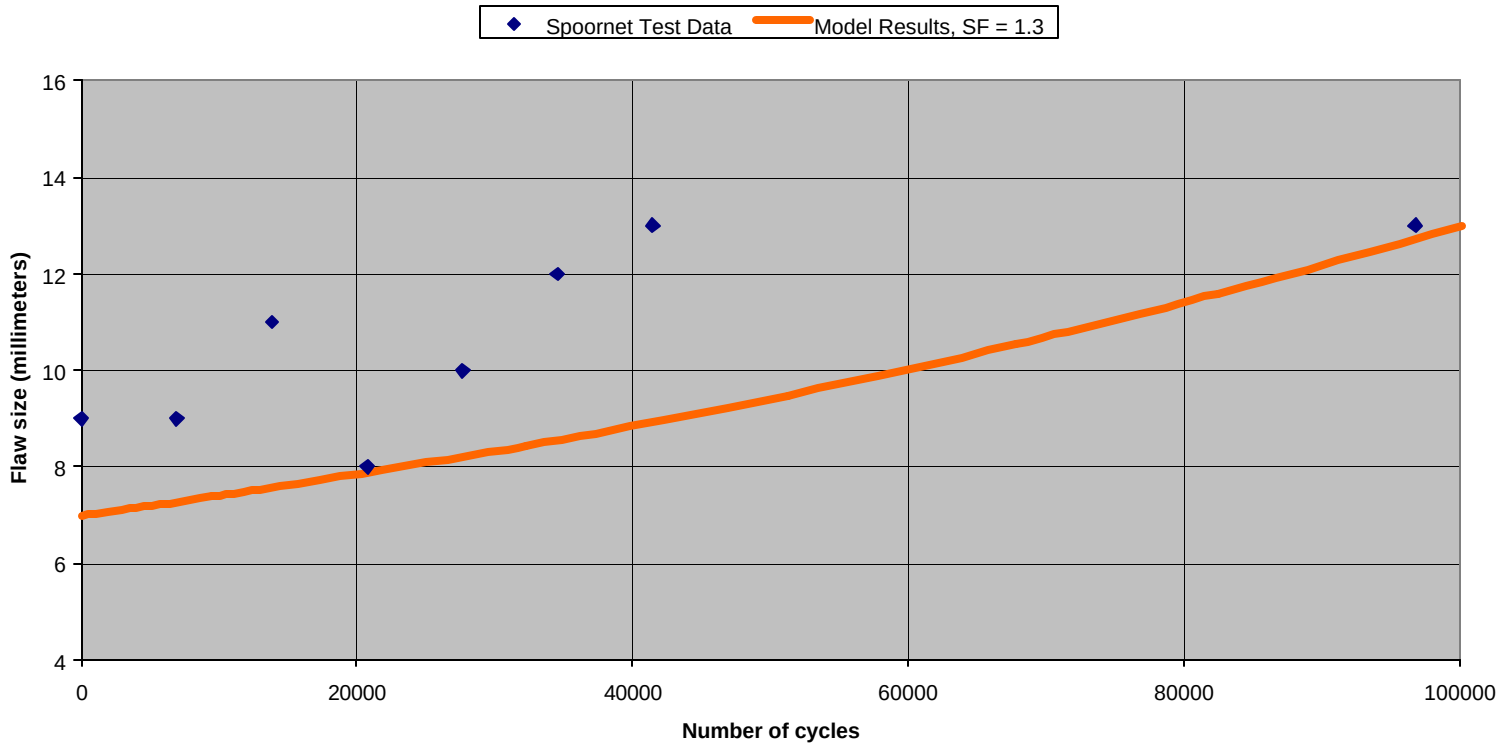

Figure C-4. Correlation between model results and Spoornet field test data for Defect No. 1456.

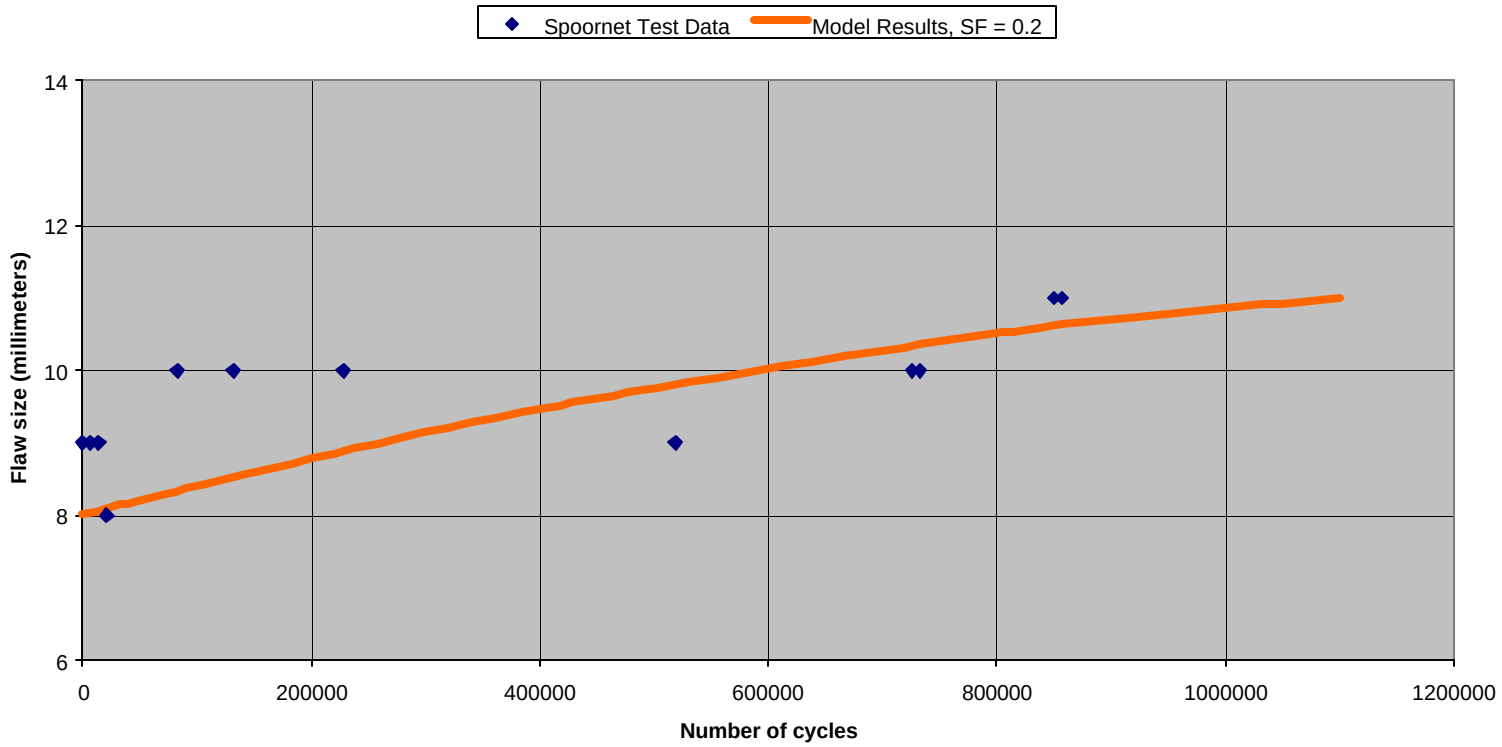

Figure C-5. Correlation between model results and Spoornet field test data for Defect No. 1601.

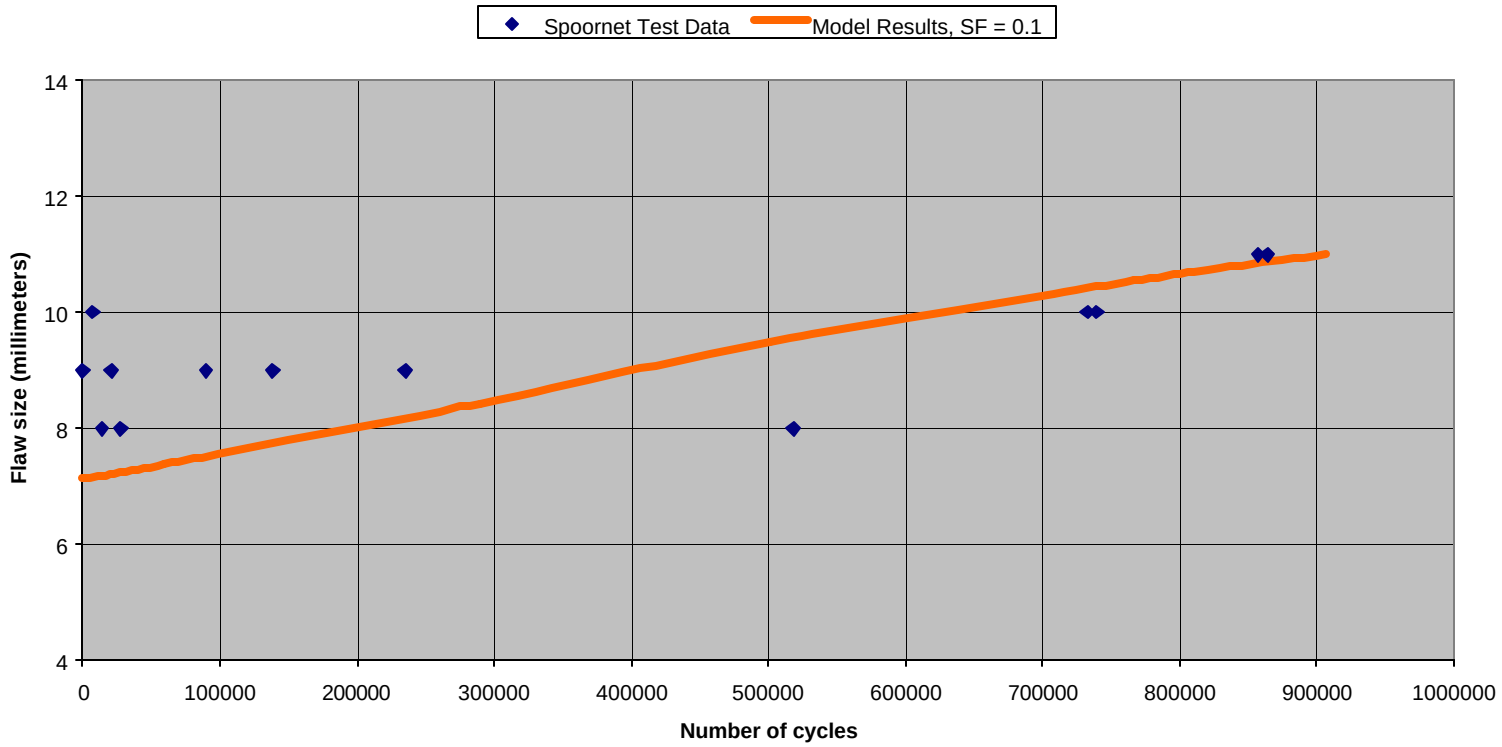

Figure C-6. Correlation between model results and Spoornet field test data for Defect No. 1614.

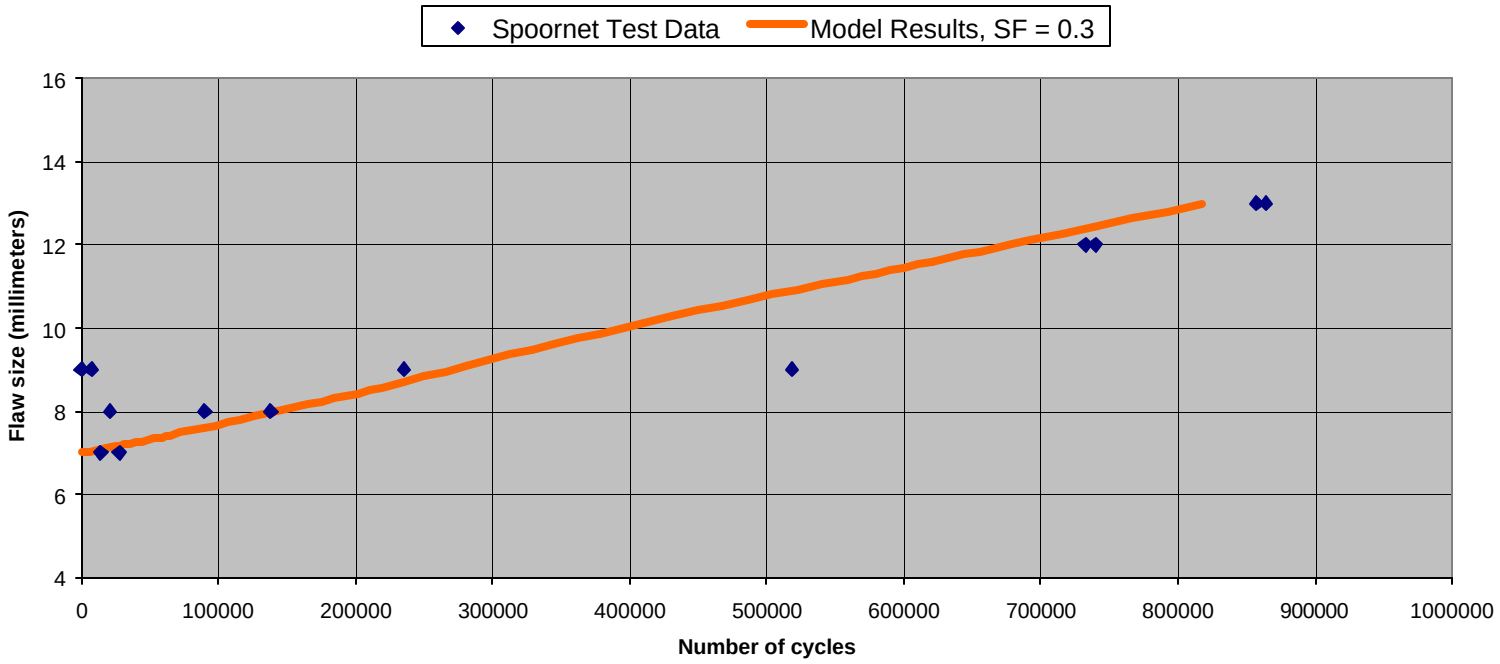

Figure C-7. Correlation between model results and Spoornet field test data for Defect No. 1628.

APPENDIX D. UNCORRELATED TEST DATA

This appendix contains data for ten defects that were not correlated with the engineering analysis model because no growth was evident. Table D-1 lists these defects along with the corresponding rail section and accumulated tonnage during the test. The data are plotted as flaw size versus tonnage in million gross tons (MGT).

Table D-1. List of Uncorrelated Defects.

Defect No.	Flaw ID	Rail Section	Tonnage (MGT)
1	3A	136 RE	142.82
2	3B	136 RE	142.82
7	7	136 RE	35.54
8	8	136 RE	35.54
9	9	136 RE	35.54
14	F6	132 RE	27.77
18	A	136 RE	23.47
21	D2	136 RE	14.72
23	F	136 RE	148.76
24	H	UIC 60	63.15

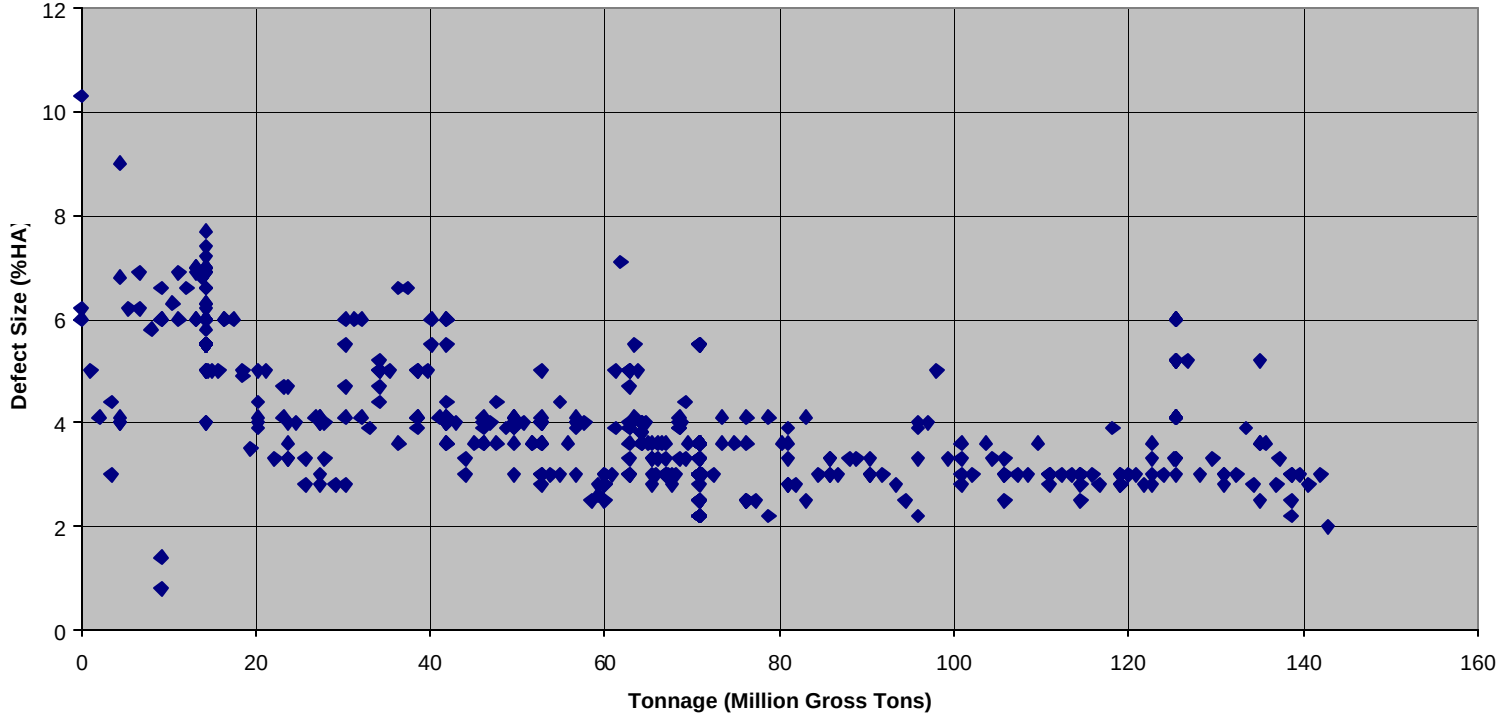

Figure D-1. FAST test data for Flaw ID 3A.

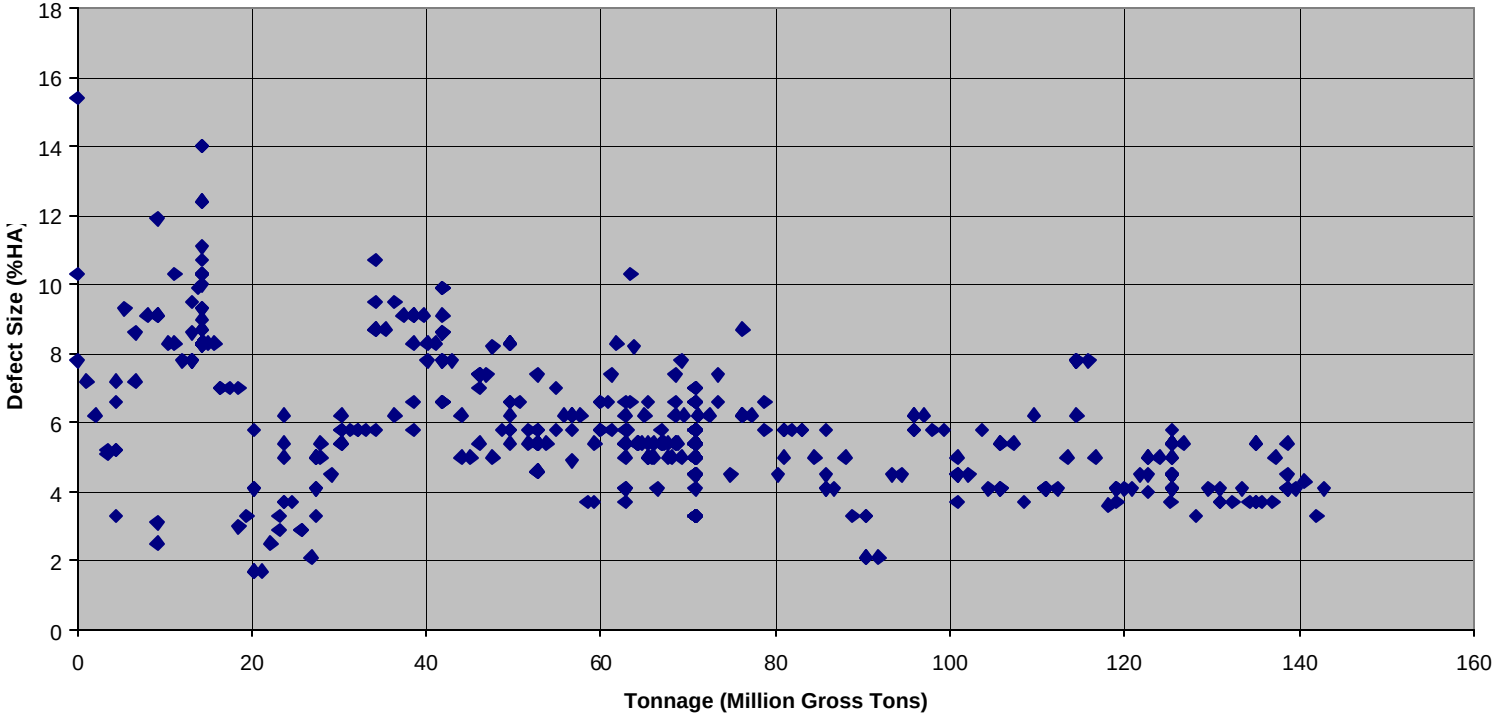

Figure D-2. FAST test data for Flaw ID 3B.

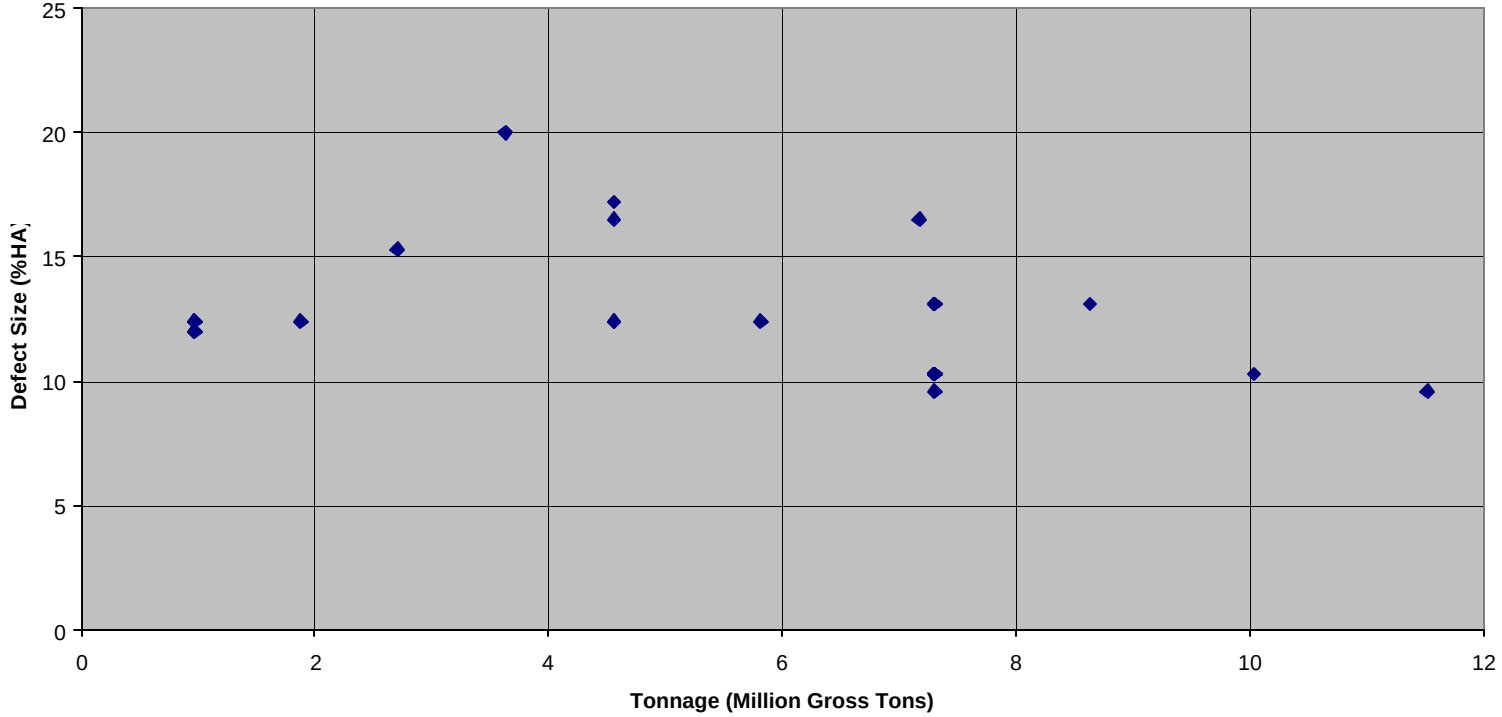

Figure D-3. FAST test data for Flaw ID 7.

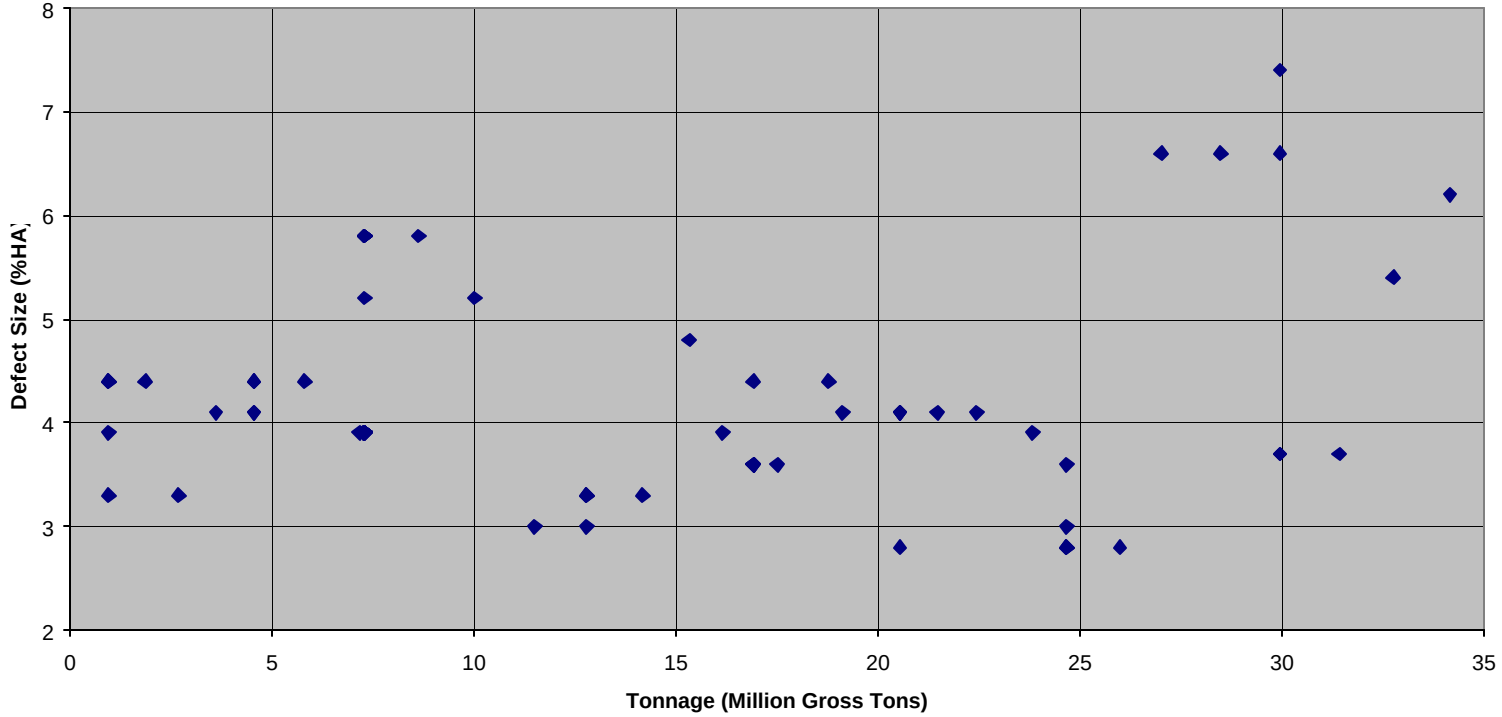

Figure D-4. FAST test data for Flaw ID 8.

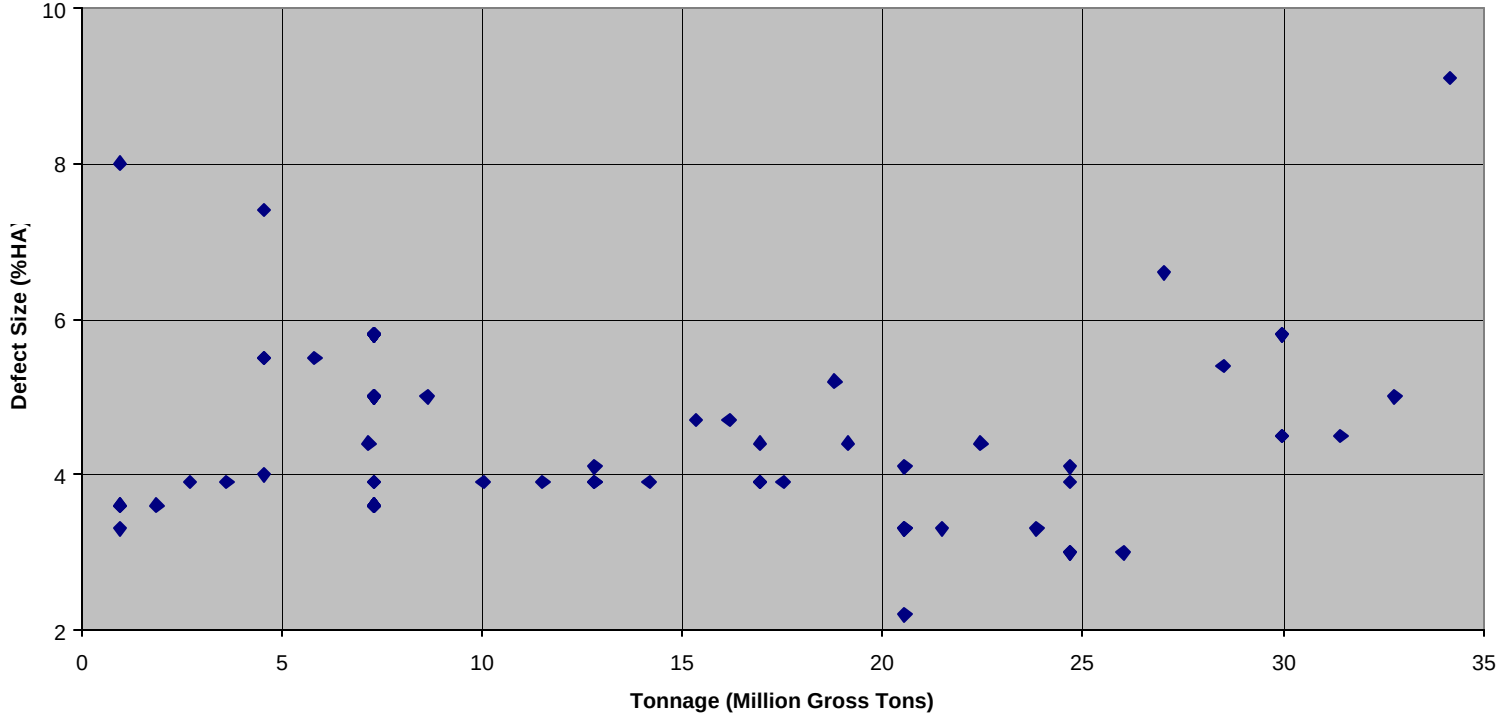

Figure D-5. FAST test data for Flaw ID 9.

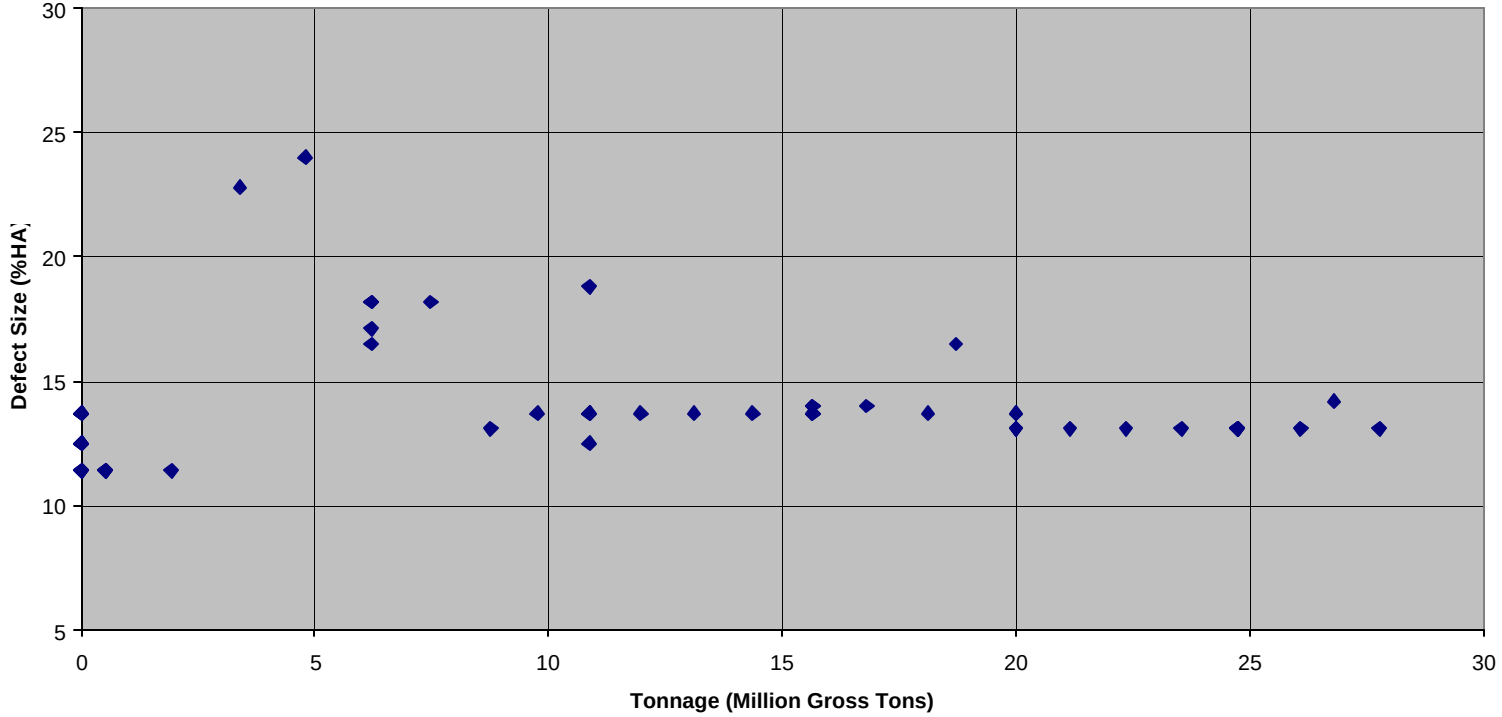

Figure D-6. FAST test data for Flaw ID F6.

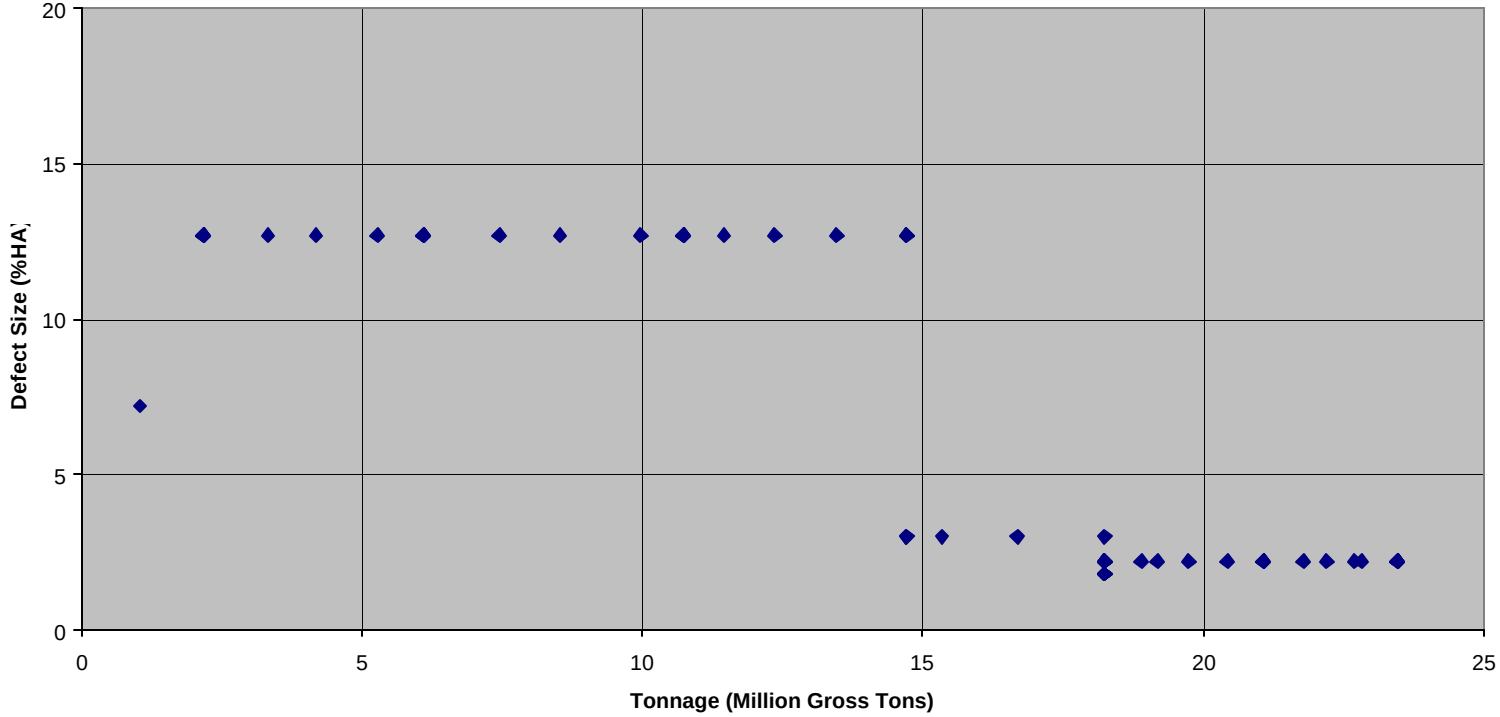

Figure D-7. FAST test data for Flaw ID A.

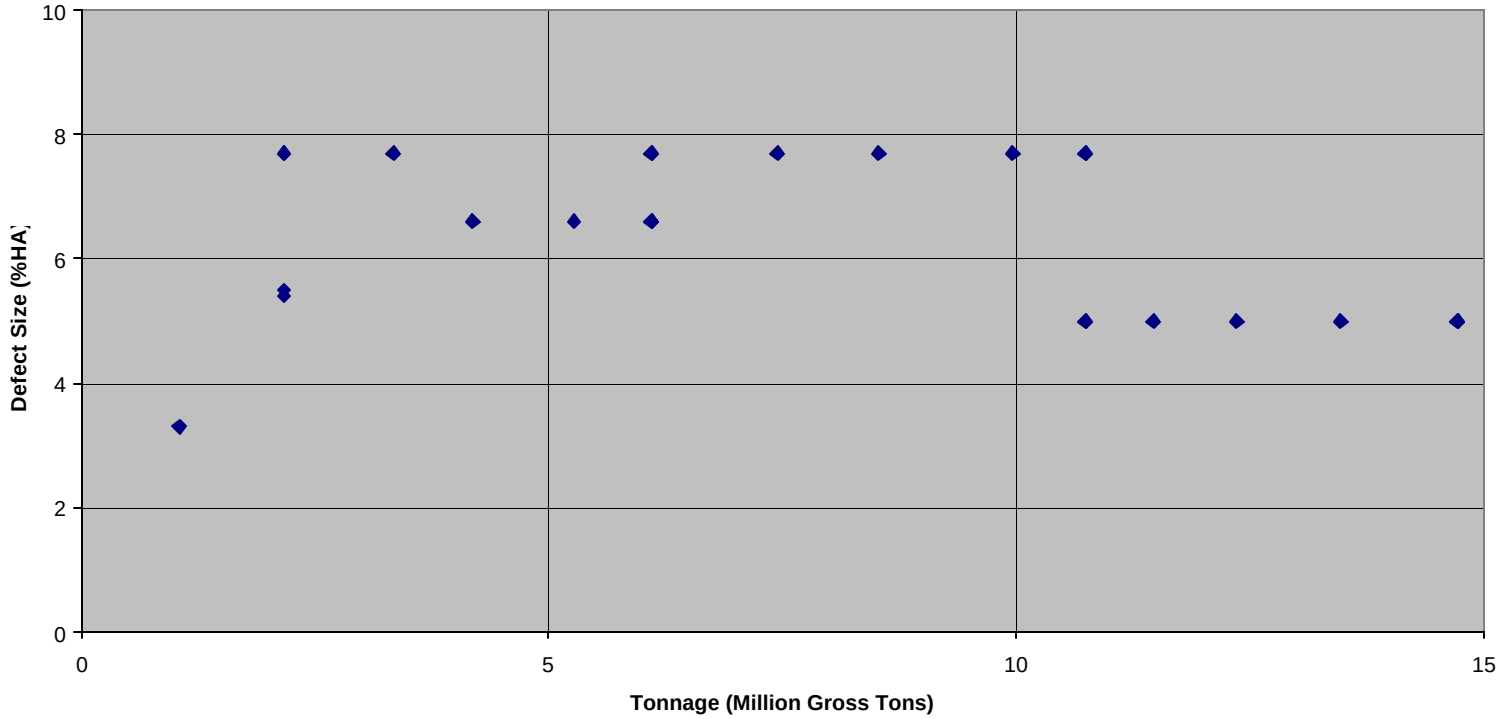

Figure D-8. FAST test data for Flaw ID D2.

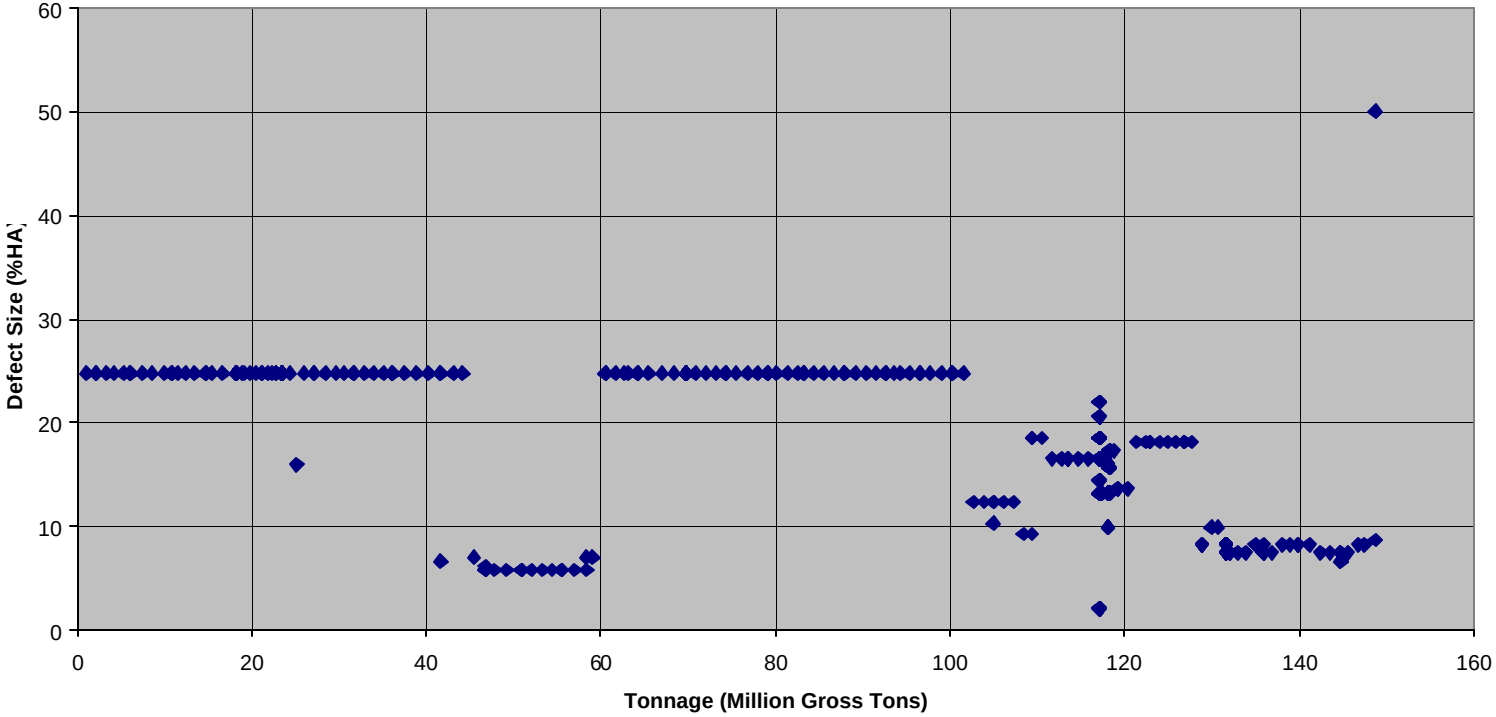

Figure D-9. FAST test data for Flaw ID F.

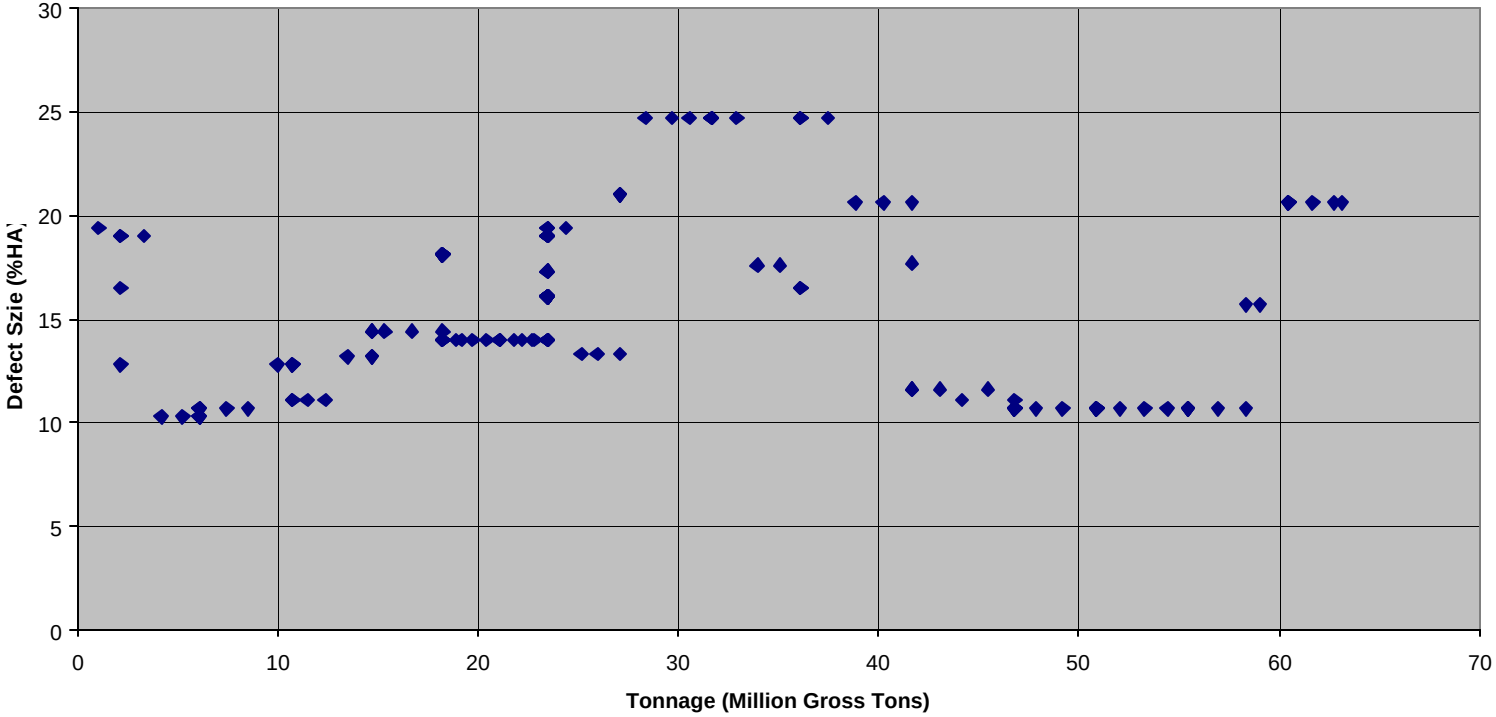

Figure D-10. FAST test data for Flaw ID H.